Semnan University

Journal of Heat and Mass Transfer Research

Journal homepage: https://jhmtr.semnan.ac.ir

ISSN: 2383-3068

Research Article

Flow of Couple-Stress and Micropolar Immiscible Liquid Layers Between Permeable Beds with Entropy Generation

Madhurya Vangalapudi [a] * and Suripeddi Srinivas [a]

[a] *Department of Mathematics, VIT-AP, Guntur, 522237, India*

ARTICLE INFO

Article history:

Received: 2025-04-02

Revised: 2025-07-25

Accepted: 2025-08-02

Keywords:

Microrotation parameter;

B-Jconditions;

Entropy generation;

Permeable bed;

Couple stress parameter.

ABSTRACT

The study explores heat and mass transfer characteristics of micropolar and couple stress liquids under the influence of an inclined magnetic field between two permeable beds. Viscous and Darcy dissipations have been accounted for in this model. In this model, the flow is divided into three regions: Region-B contains a micropolar liquid, while Region-A and C are occupied by couple stress liquids. Liquid injection occurs through the lower bed, with extraction from the upper bed at the same velocity. The Beavers-Joseph slip boundary conditions govern the liquid-permeable bed interface. The equations that govern the flow are solved numerically using the RK-4th order method in conjunction with the shooting method in Mathematica. Graphical results have been presented to illustrate the effects of pertinent parameters on velocity, microrotation, temperature, concentration, Nusselt number, entropy generation, Bejan number, and stress distribution. Our results reveal that the flow is suppressed by the Hartmann number, slip, permeability, and frequency parameters. When the Brinkman number, inclination angle, and micropolar material parameter increase, the temperature distribution also rises. However, higher Schmidt and Soret numbers contribute to a decrease in concentration, whereas a greater diffusivity ratio results in a rise in concentration. Entropy generation rises with an increase in the Brinkman number but falls with the growth of the slip parameter. Furthermore, with the rise of the permeability parameter and Hartmann number, the Nusselt number decreases at the lower permeable bed, and it shows a reverse trend at the upper permeable bed. A comparative analysis of our results with those of Nikodijevic et al. [1] and Pramod et al. [2] shows excellent agreement.

1. Introduction

Pulsating flow improves mixing, heat transfer, and system efficiency by introducing periodic variations in velocity and pressure. It is applied in biomedical devices (e.g., artificial hearts), combustion engines, and heat exchangers for optimised performance. Many studies have explored pulsatile flow in Newtonian and non-Newtonian fluids under various conditions, as documented in references [1–13] and other pertinent literature. Radhakrishnamacharya and Maiti [4] studied heat transfer during pulsatile flow in a porous channel. It was reported that at

* **Corresponding author.**
E-mail address: madhurya6699@gmail.com

Cite this article as:

Vangalapudi, M. and Srinivas, S., 2026. Flow of Couple-Stress and Micropolar Immiscible Liquid Layers Between Permeable Beds with Entropy Generation. *Journal of Heat and Mass Transfer Research*, 13(1), pp. 19-41.

https://doi.org/10.22075/JHMTR.2025.37292.1707

higher frequencies, the injection wall exhibited a phase lag, while the suction wall showed a phase lead. Additionally, it was noted that the Eckert number had no influence on the phase behaviour at either wall. Botong et al. [5] conducted a numerical study on laminar flow within a uniformly porous channel, considering suction and injection at both moving walls. Their investigation demonstrates that the characteristics of various solutions to the problem are determined numerically for both the velocity coefficient and the Reynolds number. Umavathi et al. [6] performed an analytical study on fully developed laminar flow between vertical parallel plates filled with two immiscible liquids in a composite porous medium. Their analysis revealed that the couple stress parameter enhanced flow under sparse porosity, reduced flow for moderate porosity, and decreased velocity. Moreover, dense porosity led to an increase in first-order temperature. The paper by Makinde and Tirivanhu [7] focused on the first and second laws of thermodynamics applied to flow and heat transfer within a vertical channel formed by two uniformly porous parallel plates, with suction and injection. Their findings indicate that, near the left wall subjected to fluid injection, the irreversibility from fluid friction in the presence of the magnetic field significantly outweighs the irreversibility associated with heat transfer. Samuel and Makinde [8] explored the impact of Navier slip on entropy generation within a porous channel with suction and injection. As the pressure gradient increases, the velocity at the injection wall rises, reaching its maximum at the channel centerline, and fluid temperature increases with a higher Brinkman number, showing a minimum at the injection wall and a maximum at the suction wall. Srinivas et al. [9] studied the effects of chemical reactions and Soret effects on the hydromagnetic laminar viscous pulsating flow through a porous channel under slip and convective boundary conditions. Analytical solutions are provided for velocity, temperature, and concentration. Srinivas et al. [10] examined the effects of thermal radiation, chemical reactions, and thermal diffusion on the hydromagnetic pulsating flow of Casson fluid within a porous channel. Their study results suggest that an increase in the Hartmann number and radiation parameter lowers the Nusselt number distribution at the upper wall for both Newtonian and non-Newtonian fluids. Additionally, higher values of the chemical reaction parameter and Soret number reduce the mass transfer rate at the upper wall. Umavathi and Anwar [11] conducted a numerical exploration of how thermophysical properties affect heat transfer at the interface of two immiscible fluids within a vertical duct. Their study revealed that, for small values of the Grashof number, the velocity contour appears flat in the lower half of the duct and steep in the upper half. Additionally, an increase in the viscosity ratio parameter induces flow acceleration in the upper half of the duct while causing deceleration in the lower half. Padma and Srinivas [12] analysed the pulsating flow of two immiscible, conducting, and incompressible viscous fluids in a channel filled with a porous medium, accounting for thermal radiation effects. Their study results indicate that an increase in the frequency parameter of the pressure gradient tends to induce oscillations in the unsteady velocity and temperature profiles. Additionally, as the frequency parameter rises, the velocity distribution decreases. The study by Komal and Srinivas [13] focused on the pulsatile flow behaviour of an immiscible ternary hybrid nanofluid in a corrugated, curved channel. Results from their study reveal that the optimal heat transfer occurs with molybdenum disulfide nanoparticles in an out-of-phase arrangement. Additionally, at elevated Hartmann number values, the influence of wall corrugations becomes negligible.

The heat and mass transfer in pulsating flows are crucial for enhancing transport rates in engineering systems, leveraging unsteady flow characteristics to improve efficiency. Applications include cooling systems, chemical reactors, biomedical devices, and microfluidic technologies. Extensive research has examined heat and mass transfer with entropy generation in Newtonian and non-Newtonian fluid flows, as seen in references [14–27] and related studies. Trevisan and Bejan [14] conducted an analytical and numerical study on combined heat and mass transfer through natural convection in a vertical enclosure. In their study, similarity solutions in heat-transfer-driven flows (when $Le > 1$) and mass-transfer-driven flows (when $Le < 1$) document the effect of changing the Lewis number. Numerical modelling of coupled heat and mass transfer in a square lid-driven cavity was examined by Abdalla et al. [15]. Their results illustrate the spectrum in which elevated heat and mass transfer rates can be achieved for a specific Richardson number. Umavathi et al. [16] studied the impact of a first-order chemical reaction in a vertical double-passage channel under the influence of an applied electric field. Their findings indicated that the temperature distribution is enhanced for positive and negative electric field load parameters across baffle positions. In contrast, higher chemical reaction parameters result in reduced flow in each stream at all baffle positions. The transfer of energy and mass properties of ice slurry in pulsating flow was the subject of a computational study

conducted by Cai et al. [17]. Their findings showed that ice slurry with larger particles and greater ice volume fractions exhibits enhanced heat transfer. The cycle-averaged heat transfer coefficient was found to increase with higher pulsation frequency, relative velocity amplitude, and mean velocity. Srinivas and Ramana Murthy [18] examined the entropy generation rate for the flow of immiscible micropolar fluids in a horizontal channel bounded by porous beds. They found that as viscous effects intensify, the maximum entropy generation rate shifts to the plates, where higher fluid friction causes greater irreversibility. The entropy generation in magnetohydrodynamic (MHD) pulsatile flow of Jeffrey nanofluid through a porous channel, incorporating the Cattaneo-Christov theory, is explored by Thamizharasan and Subramanyam Reddy [19]. Their study reveals that the nanofluid temperature rises with an increase in the Eckert number, thermophoretic effects, and Brownian motion. Entropy generation is found to increase with higher Eckert numbers and radiation parameters, while the Bejan number grows with an increase in the Hartmann number. Pramod and Nithisha [20] investigated entropy generation in micropolar and couple stress fluid flow through an inclined porous channel utilising the HAM. Their analysis reveals that increasing the values of couple stress can suppress the linear velocities of micropolar-couple stress fluid in an inclined porous channel. Additionally, the temperature profile within the porous channel improves as the inclination angle increases. Furthermore, entropy generation is highest near the walls where the micropolar fluid flows and lowest near the centre where the couple stress fluid flows. Their results show that increasing the Grashof number raises both velocity and temperature. The Bejan number rises with the radiation parameter for slip and no-slip scenarios, while entropy generation decreases as the magnetic field strength grows. Recently, Padma et al. [21] explored a study on entropy generation in the two-phase immiscible magnetohydrodynamic (MHD) flow of a pulsating Casson fluid through a vertical porous medium, considering slip effects. Very recently, layered non-miscible liquid flow in an inclined channel subject to a pulsatile pressure gradient has been explored by Komal and Srinivas [22]. Their results revealed that a reduction in the total velocity and concentration distributions is observed when the nanoparticle concentration increases from 1% to 3% and 5%. The utilisation of the greatest shape factor values can result in enhanced heat transfer. Vaishnav et al. [26] conducted a computational analysis of radiative micropolar fluid flow over a curved stretching sheet, accounting for viscous dissipation. Their results revealed that the local heat transfer rate at the surface decreases with an increase in the magnetic parameter, while it increases with a rise in the radiation parameter.

Permeable beds enable controlled fluid flow and filtration, playing a vital role in groundwater recharge, oil recovery, thermal management in various industries, environmental engineering, construction, energy storage, and industrial processes. Numerous studies have investigated pulsatile flow between permeable beds with suction and injection in both Newtonian and non-Newtonian fluids, as highlighted in references [28–35] and other relevant literature. Vajravelu et al. [28] studied the combined effects of free and forced convection in an inclined channel with permeable boundaries where one of the boundaries is moving. They derived mathematical expressions for velocity, temperature, pressure, mass flux, fractional increases in mass flux, and shear stress. The pulsating flow of a stratified viscous liquid with varying viscosity between permeable beds was explored by Avinash et al. [30]. In their analysis, the fluid flow is induced by an unsteady pressure gradient, with flow dynamics between and through permeable beds described by the Navier–Stokes equations and Darcy's law. The study provides analytical solutions for steady and unsteady velocities, volume flux, and fractional increases, all of which are explored and illustrated graphically. The pulsating flow of an incompressible micropolar liquid between permeable beds in the presence of an inclined, uniform magnetic field was studied by Bitla and Iyengar [33]. Deepak and Manju [34] studied MHD pulsatile flow and heat transfer of two immiscible couple stress fluids between permeable beds. Their results indicated that both velocity and temperature rise as the slip parameter increases, while both decrease with an increase in the porosity parameter. Mukherjee and Shit [35] investigated the mathematical modelling of electrothermal couple stress nanofluid flow and entropy in a porous microchannel during the injection process. Their findings indicate that the nanofluid temperature rises with an increase in the ion diffusion coefficient, whereas it decreases with enhancements in the porous medium's permeability and the couple stress parameter. Despite considerable research into flows between permeable beds, immiscible flow scenarios remain underexplored.

Motivated by previous findings, this study proposes a mathematical model for immiscible flow between permeable beds, addressing an area yet to be covered. These studies are crucial for improving the modelling of immiscible flows

by capturing micro-level stresses and particle rotations, which are essential in fields like enhanced oil recovery, microfluidics, biomedical engineering, chemical processing, and environmental remediation. Future research could explore non-Newtonian fluid dynamics under time-varying boundary conditions or pulsating flows, expand to three-dimensional studies, integrate thermal radiation effects, and utilise machine learning for parameter optimisation and predictive enhancement. This model investigates heat and mass transfer in micropolar and couple stress liquids under an inclined magnetic field, accounting for viscous and Darcy dissipations. It considers a system where couple-stress liquid layers (Region−A and C) are separated by a micropolar liquid layer (Region−B) between two permeable beds. The liquid is introduced through the lower permeable bed at a prescribed velocity and withdrawn from the upper bed at an equivalent rate. The B−J slip boundary conditions [34] govern the fluid-permeable bed interface. The flow equations are numerically solved using the fourth-order Runge-Kutta (RK-4) method combined with the shooting technique implemented in Mathematica. The results are presented in graphical form for analysis and interpretation.

2. Mathematical Framework

Consider the motion of three immiscible liquid flow layers between permeable beds under an applied inclined magnetic field. The flow between permeable beds is divided into three distinct regions: A, B, and C, which are subjected to an inclined magnetic field, as given in Figure 1. The velocity, temperature, and concentrations of Regions - A, B, and C are u_j, θ_j, Φ_j where $j = 1, 2, 3$ respectively. Region A $(-h \le y \le 0)$ is occupied by a couple-stress liquid [34, 37], Region B $(0 \le y \le \delta)$ is filled with a micropolar liquid [31,33,38,39,40,41], and Region C $(\delta \le y \le 2h)$ contains a couple-stress liquid. This analysis relies on the following assumptions:

i). The liquids are to be incompressible and immiscible.

ii). The permeable beds are considered to be rigid and uniform in structure.

iii). The flow is unsteady, fully developed, and exhibits laminar characteristics.

iv). The motion of the liquid is subjected to a periodic pressure gradient in a specific form.

Since the flow is fully developed, which means $\frac{\partial u}{\partial x} = 0$, i.e., u is solenoidal, which results in $\frac{\partial v}{\partial y} = 0$. Thus, the velocity, v, does not change in any section of the channel. Since the beds are porous with constant suction and injection, v is V (is constant). The equation of momentum in the direction of the y −axis is reduced to $\frac{\partial p}{\partial y} = 0$.

Darcy's law is a fundamental principle for describing flow through porous media with minimal permeability. It is widely recognised as the simplest and most extensively applied model, establishing that the fluid's filtration velocity is proportional to the difference between the body force and the pressure gradient. In 1856, French engineer Henry Darcy conducted experiments to study water flow through a vertical column of homogeneous sand. These experiments revealed a proportional relationship between the water flow rate q, the applied pressure difference ∇P, and other factors, expressed as: $\bar{q} = -\frac{K}{\mu}\nabla P$.

For flows near impermeable surfaces, the no-slip condition typically applies at the boundary. However, for permeable surfaces, this condition breaks down due to the tangential migration of liquid within the porous medium. In such cases, the liquid exhibits slip behaviour along the boundary inside the porous structure, invalidating the no-slip condition. Through experimental investigations, Beavers and Joseph (BJ) demonstrated that velocity slip is related to tangential stress, formalised as the BJ condition: $\frac{dU}{dy} = \frac{\alpha}{\sqrt{k}}(U_B - Q)$[36]. In this equation, U_B represents the slip velocity, Q the velocity within the porous bed, K the permeability, and α the slip coefficient. When $\alpha = 0$, the condition represents perfect slip. Conversely, as $\alpha \to \infty$, the no-slip condition is recovered $(U_B = Q)$. Additionally, as $K \to \infty$, the surface behaves as impermeable, leading to zero normal velocity at the interface.

Here, $Q_1 = -(K_1/\mu_1)\,(\partial p/\partial x)$ and $Q_2 = -(K_2/\mu_3)(\partial p/\partial x)$ are Darcy velocities for the lower and upper permeable beds, respectively.

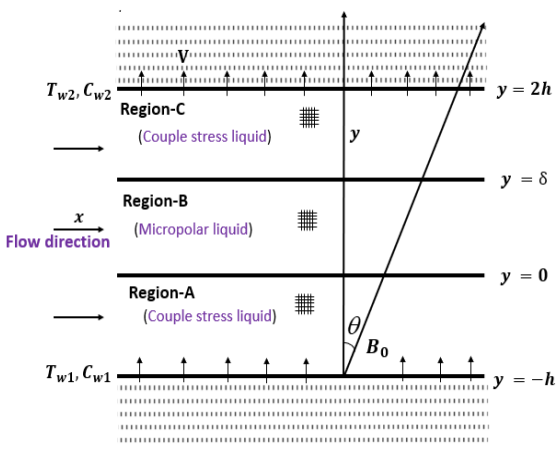

Fig. 1. Schematic flow

The governing flow equations are :

- **Region-A**

$$\rho_1\left(\frac{\partial u_1}{\partial t}+V\frac{\partial u_1}{\partial y}\right)=-\frac{\partial p}{\partial x}+\mu_1\frac{\partial^2 u_1}{\partial y^2}-\eta_1\frac{\partial^4 u_1}{\partial y^4}$$
$$-\sigma_{*1}(B_o Cos\theta)^2 u_1-\frac{\mu_1}{k_1}u_1. \quad (1)$$

$$\rho_1 cp_1\left(\frac{\partial T_1}{\partial t}+V\frac{\partial T_1}{\partial y}\right)=K_1\frac{\partial^2 T_1}{\partial y^2}+\mu_1\left(\frac{\partial u_1}{\partial y}\right)^2$$
$$+\eta_1\left(\frac{\partial^2 u_1}{\partial y^2}\right)^2+\frac{\mu_1}{k_1}u_1^2. \quad (2)$$

$$\left(\frac{\partial C_1}{\partial t}+V\frac{\partial C_1}{\partial y}\right)=D_1\frac{\partial^2 C_1}{\partial y^2}+\frac{D_1K_1}{T}\frac{\partial^2 T_1}{\partial y^2}. \quad (3)$$

- **Region-B**

$$\rho_2\left(\frac{\partial u_2}{\partial t}+V\frac{\partial u_2}{\partial y}\right)=-\frac{\partial P}{\partial x}+(\mu_2+k)\frac{\partial^2 u_2}{\partial y^2}$$
$$+k\frac{\partial N}{\partial y}-\sigma_{*2}(B_o Cos\theta)^2 u_2-\frac{\mu_2+k}{k_2}u_2. \quad (4)$$

$$\rho_2 j\left(\frac{\partial N}{\partial t}+\frac{\partial N}{\partial y}\right)=-2kN-k\frac{\partial u_2}{\partial y}+\gamma\frac{\partial^2 N}{\partial y^2}.$$

$$\rho_2 cp_2\left(\frac{\partial T_2}{\partial t}+V\frac{\partial T_2}{\partial y}\right)=K_2\frac{\partial^2 T_2}{\partial y^2}+\mu_2\left(\frac{\partial u_2}{\partial y}\right)^2$$
$$+k\left(\frac{\partial u_2}{\partial y}+2N\right)^2+\beta_1\left(\frac{\partial N}{\partial y}\right)^2+\frac{(\mu_2+k)}{k_2}u_2^2. \quad (5)$$

$$\left(\frac{\partial C_2}{\partial t}+V\frac{\partial C_2}{\partial y}\right)=D_2\frac{\partial^2 C_2}{\partial y^2}+\frac{D_2K_2}{T}\frac{\partial^2 T_2}{\partial y^2}. \quad (6)$$

- **Region-C**

$$\rho_3\left(\frac{\partial u_3}{\partial t}+V\frac{\partial u_3}{\partial y}\right)=-\frac{\partial p}{\partial x}+\mu_3\frac{\partial^2 u_3}{\partial y^2}$$
$$-\eta_2\frac{\partial^4 u_3}{\partial y^4}-\sigma_{*3}(B_o Cos\theta)^2 u_3-\frac{\mu_3}{k_3}u_3. \quad (7)$$

$$\rho_3 cp_3\left(\frac{\partial T_3}{\partial t}+V\frac{\partial T_3}{\partial y}\right)=K_3\frac{\partial^2 T_3}{\partial y^2}$$
$$+\mu_3\left(\frac{\partial u_3}{\partial y}\right)^2+\eta_2\left(\frac{\partial^2 u_3}{\partial y^2}\right)^2+\frac{\mu_1}{k_1}u_3^2. \quad (8)$$

$$\left(\frac{\partial C_3}{\partial t}+V\frac{\partial C_3}{\partial y}\right)=D_3\frac{\partial^2 C_3}{\partial y^2}+\frac{D_3K_3}{T}\frac{\partial^2 T_3}{\partial y^2}. \quad (9)$$

Boundary conditions for velocity

$$\left.\begin{aligned}
&\frac{\partial u_1}{\partial y}=\frac{\alpha}{\sqrt{K_{*1}}}\left(u_1'-Q_1\right),u_1'=u_1,\\
&\frac{\partial^2 u_1}{\partial y^2}=0,\quad \text{at}\quad y=-h.\\
&\mu_1\frac{\partial u_1}{\partial y}-\eta_1\frac{\partial^3 u_1}{\partial y^3}=(\mu_2+k)\frac{\partial u_2}{\partial y}+kN,\\
&N=0,u_1=u_2,\frac{\partial u_1}{\partial y}=\frac{\partial u_2}{\partial y},\quad \text{at}\quad y=0.\\
&\frac{\partial^3 u_3}{\partial y^3}=(\mu_2+k)\frac{\partial u_2}{\partial y}+kN,N=0,\\
&u_2=u_3,\frac{\partial u_2}{\partial y}=\frac{\partial u_3}{\partial y},\quad \text{at}\quad y=\delta.\\
&\frac{\partial u_3}{\partial y}=-\frac{\alpha}{\sqrt{K_{*2}}}\left(u_3'-Q_2\right),u_3'=u_3,\\
&\frac{\partial^2 u_3}{\partial y^2}=0,\quad \text{at}\quad y=2h.
\end{aligned}\right\} \quad (10)$$

Boundary conditions for temperature

$$\left.\begin{aligned}
&T_1=T_{w1},\quad \text{at}\quad y=-h.\\
&T_1=T_2,k_1\frac{\partial T_1}{\partial y}=k_2\frac{\partial T_2}{\partial y},\quad \text{at}\quad y=0.\\
&T_2=T_3,k_2\frac{\partial T_2}{\partial y}=k_3\frac{\partial T_3}{\partial y},\quad \text{at}\quad y=\delta.\\
&T_3=T_{w2},\quad \text{at}\quad y=2h.
\end{aligned}\right\} \quad (11)$$

Boundary conditions for concentration

$$\left.\begin{aligned}
&C_1=C_{w1},\quad \text{at}\quad y=-h.\\
&C_1=C_2,D_1\frac{\partial C_1}{\partial y}=D_2\frac{\partial C_2}{\partial y},\quad \text{at}\quad y=0.\\
&C_2=C_3,D_2\frac{\partial C_2}{\partial y}=D_3\frac{\partial C_3}{\partial y},\quad \text{at}\quad y=\delta.\\
&C_3=C_{w2},\quad \text{at}\quad y=2h.
\end{aligned}\right\} \quad (12)$$

Non-dimensional flow quantities:

$$
\left.
\begin{aligned}
&x^* = \frac{x}{h}, y^* = \frac{y}{h}, u_j{}^* = \frac{uj}{V}, N^* = \frac{Nh}{V},\\
&t^* = \frac{tV}{h}, \omega^* = \frac{\omega h}{V}, p^* = \frac{p}{\rho V^2}, n = \frac{kh^2}{\gamma},\\
&\theta_j{}^* = \frac{T_j - T_{w1}}{T_{w2} - T_{w1}}, \Phi_j{}^* = \frac{C_j - C_{w1}}{C_{w2} - C_{w1}}, S_j = \frac{\mu_j h^2}{\eta_j},\\
&Z_{k1} = \frac{k_2}{k_1}, Z_{k2} = \frac{k_3}{k_1}, Z_k = Z_{k1} = Z_{k2}, \sigma_4 = h/\sqrt{K_{*1}},\\
&Z_{D1} = \frac{D_2}{D_1}, Z_{D2} = \frac{D_3}{D_2}, Z_D = Z_{D1} = Z_{D2}, \sigma 5 = h/\sqrt{K_{*2}},\\
&Z_{\rho 1} = \frac{\rho_2}{\rho_1}, Z_{\rho 2} = \frac{\rho_3}{\rho_2}, m = \frac{k}{\mu_2}, Z_\rho = Z_{\rho 1} = Z_{\rho 2},\\
&Z_\sigma = \sigma_4{}^2 = \sigma_5{}^2, \sigma_1 = h/\sqrt{\kappa_1}, \Lambda = \frac{Rg_j DC_{w1}}{K_1},\\
&\sigma_2 = h/\sqrt{\kappa_2}, \sigma_3 = h/\sqrt{\kappa_3}, M_1 = B_o h\sqrt{\frac{\sigma_{*1}}{\rho_1 \upsilon_1}},\\
&M_2 = B_o h\sqrt{\frac{\sigma_{*2}}{\mu_2 + k}}, M_3 = B_o h\sqrt{\frac{\sigma_{*3}}{\rho_3 \upsilon_3}}, R_1 = \frac{\rho_1 uh}{\mu_1},\\
&R_{\partial} = \frac{\rho_2 uh}{\mu_2 + k}, R_3 = \frac{\rho_3 uh}{\mu_3}, P_j = \frac{j(\mu_2 + k)}{\gamma}, \Pi = \frac{\Delta C}{C_{w1}},\\
&\mathrm{Pr} = \frac{\mu_1 C_p}{k_1}, Br = \frac{\mu_1 V^2}{k_1 \Delta T}, Sc = \frac{\mu_1}{\rho_1 D_1}, Sr = \frac{D\Delta T}{TVh\Delta C},\\
&Z_\beta = \frac{\beta_1}{\mu_2 h^2}, \Omega = \frac{\Delta T}{T_{w1}}, \sigma = \sigma_1{}^2 = \sigma_2{}^2 = \sigma_3{}^2, \delta_1 = \frac{\delta}{h}.
\end{aligned}
\right\} \quad (13)
$$

After dropping asterisks:

- **Region-A**

$$\frac{\partial^4 u_1}{\partial y^4} - S_1 \frac{\partial^2 u_1}{\partial y^2} + R_1 S_1 \left(\frac{\partial u_1}{\partial t} + \frac{\partial u_1}{\partial y} \right) + S_1 \left(M_1 Cos\theta \right)^2 u_1 + S_1 \sigma_1{}^2 u_1 - S_1 R_1 \left(\frac{\partial P}{\partial x} \right) = 0. \quad (14)$$

$$\frac{\partial^2 \theta_1}{\partial y^2} + Br \left(\frac{\partial u_1}{\partial y} \right)^2 + \frac{Br}{S_1} \left(\frac{\partial^2 u_1}{\partial y^2} \right)^2 - R_1 \mathrm{Pr} \left(\frac{\partial \theta_1}{\partial t} + \frac{\partial \theta_1}{\partial y} \right) + Br \sigma_1{}^2 u_1{}^2 = 0. \quad (15)$$

$$\frac{1}{Sc} \frac{\partial^2 \Phi_1}{\partial y^2} + Sr \frac{\partial^2 \theta_1}{\partial y^2} - R_1 \left(\frac{\partial \Phi_1}{\partial t} + \frac{\partial \Phi_1}{\partial y} \right) = 0. \quad (16)$$

- **Region-B**

$$\frac{\partial^2 u_2}{\partial y^2} + m \frac{\partial N}{\partial y} - R_2 \left(\frac{\partial u_2}{\partial t} + \frac{\partial u_2}{\partial y} \right) - \left(\left(M_2 Cos\theta \right)^2 + \sigma_2{}^2 \right) u_2 - R_2 \left(\frac{\partial P}{\partial x} \right) = 0. \quad (17)$$

$$\frac{\partial^2 N}{\partial y^2} - n \frac{\partial u_2}{\partial y} - R_2 P_j \left(\frac{\partial N}{\partial t} + \frac{\partial N}{\partial y} \right) - 2nN = 0.$$

$$R_2 \mathrm{Pr} \left(\frac{\partial \theta_2}{\partial t} + \frac{\partial \theta_2}{\partial y} \right) = \frac{z_{k1}}{z_{\mu 1}} \frac{\partial^2 \theta_2}{\partial y^2} + Br \left(\frac{\partial u_2}{\partial y} \right)^2 + mBr \left(\frac{\partial u_2}{\partial y} + 2N \right)^2 Z_\beta Br \left(\frac{\partial N}{\partial y} \right)^2 + (1+m) Br \sigma_2{}^2 u_2{}^2. \quad (18)$$

$$\frac{1}{Sc} \frac{\partial^2 \Phi_2}{\partial y^2} + Sr \frac{\partial^2 \theta_2}{\partial y^2} - R_2 \left(\frac{\partial \Phi_2}{\partial t} + \frac{\partial \Phi_2}{\partial y} \right) = 0. \quad (19)$$

- **Region-C**

$$\frac{\partial^4 u_3}{\partial y^4} - S_2 \frac{\partial^2 u_3}{\partial y^2} + R_3 S_2 \left(\frac{\partial u_3}{\partial t} + \frac{\partial u_3}{\partial y} \right) + S_2 \left(M_3 Cos\theta \right)^2 u_3 + S_2 \sigma_3{}^2 u_3 - S_2 R_3 \left(\frac{\partial P}{\partial x} \right) = 0. \quad (20)$$

$$\frac{z_{k2}}{z_{\mu 2}} \frac{\partial^2 \theta_3}{\partial y^2} + Br \left(\frac{\partial u_3}{\partial y} \right)^2 + \frac{Br}{S_2 z_{\mu 3}} \left(\frac{\partial^2 u_3}{\partial y^2} \right)^2 - R_3 \mathrm{Pr} \left(\frac{\partial \theta_3}{\partial t} + \frac{\partial \theta_3}{\partial y} \right) + Br \sigma_3{}^2 u_3{}^2 = 0. \quad (21)$$

$$\frac{1}{Sc} \frac{\partial^2 \Phi_3}{\partial y^2} + Sr \frac{\partial^2 \theta_3}{\partial y^2} - R_3 \left(\frac{\partial \Phi_3}{\partial t} + \frac{\partial \Phi_3}{\partial y} \right) = 0. \quad (22)$$

$$
\left.
\begin{aligned}
&\frac{\partial u_1}{\partial y} = \alpha \sigma_1 \left(u_1{}' - \frac{R_1}{\sigma_1^2} P \right), u_1{}' = u_1,\\
&\frac{\partial^2 u_1}{\partial y^2} = 0, \quad \text{at} \quad y = -1.\\
&z_{\mu 1} \frac{\partial u_1}{\partial y} - \frac{z_{\mu 1}}{S_1} \frac{\partial^3 u_1}{\partial y^3} = (1+m) \frac{\partial u_2}{\partial y} + mN, N = 0,\\
&u_1 = u_2, \frac{\partial u_1}{\partial y} = \frac{\partial u_2}{\partial y}, \quad \text{at} \quad y = 0.\\
&z_{\mu 2} \frac{\partial u_3}{\partial y} - \frac{z_{\mu 2}}{S_2} \frac{\partial^3 u_3}{\partial y^3} = (1+m) \frac{\partial u_2}{\partial y} + mN, N = 0,\\
&u_2 = u_3, \frac{\partial u_2}{\partial y} = \frac{\partial u_3}{\partial y}, \quad \text{at} \quad y = \delta_1.\\
&\frac{\partial u_3}{\partial y} = -\alpha \sigma_2 \left(u_3{}' - Z_{\rho 1} \frac{R_3}{\sigma_2^2} P \right), u_3{}' = u_3,\\
&\frac{\partial^2 u_3}{\partial y^2} = 0, \quad \text{at} \quad y = 2.
\end{aligned}
\right\} \quad (23)
$$

In view of the pulsatile pressure gradient $-\frac{\partial p}{\partial x} = \left(\frac{\partial p}{\partial x} \right)_s + \left(\frac{\partial p}{\partial x} \right)_o e^{i\omega t}$, we assume the velocity, temperature and concentration as follows:

$$\left.\begin{aligned} u_j &= u_{j1} + u_{j2}e^{i\omega t}, j = 1,2,3. \\ N &= N_s + N_o e^{i\omega t}. \\ \theta_j &= \theta_{j1} + \theta_{j2}e^{i\omega t}. \\ \Phi_j &= \Phi_{j1} + \Phi_{j2}e^{i\omega t}. \end{aligned}\right\} \quad (24)$$

Steady flow equations and boundary conditions are:

- **Region-A**

$$\frac{d^4u_{11}}{dy^4} - S_1\frac{d^2u_{11}}{dy^2} + R_1S_1\frac{du_{11}}{dy} + S_1(M_1C\cos\theta)^2u_{11} + S_1\sigma_1^2u_{11} - S_1R_1P_s = 0. \quad (25)$$

$$R_1Pr\frac{\partial\theta_{11}}{\partial y} = \frac{\partial^2\theta_{11}}{\partial y^2} + \frac{Br}{S_1}\left(\frac{\partial^2u_{11}}{\partial y^2}\right)^2 + Br\left(\frac{\partial u_{11}}{\partial y}\right)^2 + Br\sigma_1^2u_{11}^2. \quad (26)$$

$$\frac{1}{Sc}\frac{\partial^2\Phi_{11}}{\partial y^2} + Sr\frac{\partial^2\theta_{11}}{\partial y^2} - R_1\frac{\partial\Phi_{11}}{\partial y} = 0. \quad (27)$$

- **Region-B**

$$\frac{d^2u_{21}}{dy^2} + m\frac{dN_s}{dy} - R_2\frac{du_{21}}{dy} - \left(\left(M_2Cos\theta\right)^2 + \sigma_2^2\right)u_{21} - Z_{\rho1}R_2P_s = 0. \quad (28)$$

$$\frac{d^2N_s}{dy^2} - n\frac{du_{21}}{dy} - R_2P_j\frac{dN_s}{dy} - 2nN_s = 0.$$

$$R_2\,\mathrm{Pr}\left(\frac{\partial\theta_{21}}{\partial y}\right) = \frac{z_{k1}}{z_{\mu1}}\frac{\partial^2\theta_{21}}{\partial y^2} + Br\left(\frac{\partial u_{21}}{\partial y}\right)^2 + mBr\left(\frac{\partial^2u_{21}}{\partial y^2} + 4N_s^2 + 4\frac{\partial u_{21}}{\partial y}N_s\right) + Z_\beta Br\frac{\partial N_s}{\partial y} + (1+m)Br\sigma_2^2u_{21}^2. \quad (29)$$

$$\frac{1}{Sc}\frac{\partial^2\Phi_{21}}{\partial y^2} + Sr\frac{\partial^2\theta_{21}}{\partial y^2} - R_1\frac{\partial\Phi_{21}}{\partial y} = 0. \quad (30)$$

- **Region-C**

$$\frac{d^4u_{31}}{dy^4} - S_2\frac{d^2u_{31}}{dy^2} + R_3S_2\frac{du_{31}}{dy} + S_2\left(M_3Cos\theta\right)^2u_{31} + S_2\sigma_3^2u_{31} - Z_{\rho2}S_2R_3P_o = 0. \quad (31)$$

$$R_3Pr\frac{\partial\theta_{31}}{\partial y} = \frac{z_{k2}}{z_{\mu2}}\frac{\partial^2\theta_{31}}{\partial y^2} + \frac{Br}{S_2}\left(\frac{\partial^2u_{31}}{\partial y^2}\right)^2 + Br\left(\frac{\partial u_{31}}{\partial y}\right)^2 + Br\sigma_3^2u_{31}^2. \quad (32)$$

$$\frac{1}{Sc}\frac{\partial^2\Phi_{31}}{\partial y^2} + Sr\frac{\partial^2\theta_{31}}{\partial y^2} - R_3\frac{\partial\Phi_{31}}{\partial y} = 0. \quad (33)$$

$$\left.\begin{aligned} &\frac{\partial u_{11}}{\partial y} = \alpha\sigma_4\left(u_{11}' - \frac{R_1}{\sigma_4^2}P_s\right), u_{11}' = u_{11}, \\ &\frac{\partial^2u_{11}}{\partial y^2} = 0, \quad \text{at} \quad y = -1. \\ &z_{\mu1}\frac{\partial u_{11}}{\partial y} - (1/S_1)z_{\mu1}\frac{\partial^3u_{11}}{\partial y^3} = (1+m)\frac{\partial u_{21}}{\partial y} + mN_s, \\ &N_s = 0, u_{11} = u_{21}, \frac{\partial u_{11}}{\partial y} = \frac{\partial u_{21}}{\partial y}, \quad \text{at} \quad y = 0. \\ &z_{\mu2}\frac{\partial u_{31}}{\partial y} - (1/S_2)z_{\mu2}\frac{\partial^3u_{31}}{\partial y^3} = (1+m)\frac{\partial u_{21}}{\partial y} + mN_s, \\ &N_s = 0, u_{21} = u_{31}, \frac{\partial u_{21}}{\partial y} = \frac{\partial u_{31}}{\partial y}, \quad \text{at} \quad y = \delta_1. \\ &\frac{\partial u_{31}}{\partial y} = -\alpha\sigma_5\left(u_{31}' - Z_{\rho1}\frac{R_3}{\sigma_5^2}P_s\right), u_{31}' = u_{31}, \\ &\frac{\partial^2u_{31}}{\partial y^2} = 0, \quad \text{at} \quad y = 2. \end{aligned}\right\} \quad (34)$$

Temperature Steady flow Boundary conditions

$$\left.\begin{aligned} &\theta_{11} = 0, \quad \text{at} \quad y = -1. \\ &\theta_{11} = \theta_{21}, \frac{\partial\theta_{11}}{\partial y} = Z_{k1}\frac{\partial\theta_{21}}{\partial y}, \quad \text{at} \quad y = 0. \\ &\theta_{21} = \theta_{31}, \frac{\partial\theta_{21}}{\partial y} = Z_{k2}\frac{\partial\theta_{31}}{\partial y}, \quad \text{at} \quad y = 1. \\ &\theta_{31} = 1, \quad \text{at} \quad y = 2. \end{aligned}\right\} \quad (35)$$

Steady flow Concentration Boundary conditions

$$\left.\begin{aligned} &\Phi_{11} = 0, \quad \text{at} \quad y = -1. \\ &\Phi_{11} = \Phi_{21}, \frac{\partial\Phi_{11}}{\partial y} = Z_{D1}\frac{\partial\Phi_{21}}{\partial y}, \quad \text{at} \quad y = 0. \\ &\Phi_{21} = \Phi_{31}, \frac{\partial\Phi_{21}}{\partial y} = Z_{D2}\frac{\partial\Phi_{31}}{\partial y}, \quad \text{at} \quad y = \delta_1. \\ &\Phi_{31} = 1, \quad \text{at} \quad y = 2. \end{aligned}\right\} \quad (36)$$

Oscillatory flow equations and boundary conditions are:

- **Region-A**

$$\frac{d^4u_{12}}{dy^4} - S_1\frac{d^2u_{12}}{dy^2} + R_1S_1\frac{du_{12}}{dy} + R_1S_1i\omega u_{12} + S_1(M_1\cos\theta)^2u_{12} + S_1\sigma_1^2u_{12} - S_1R_1P_o = 0. \quad (37)$$

$$\frac{1}{\Pr}\frac{\partial^2\theta_{12}}{\partial y^2} + \frac{Ec}{S_1}\left(\frac{\partial^2u_{12}}{\partial y^2}\right)^2 + Ec\left(\frac{\partial u_{12}}{\partial y}\right)^2 - R_1\frac{\partial\theta_{12}}{\partial y} - R_1i\omega\theta_{12} + Ec\sigma_1^2u_{12}^2 = 0. \quad (38)$$

$$\frac{1}{Sc}\frac{\partial^2\Phi_{12}}{\partial y^2} + Sr\frac{\partial^2\theta_{12}}{\partial y^2} - R_1\frac{\partial\Phi_{12}}{\partial y} - R_1i\omega\Phi_{12} = 0. \quad (39)$$

- **Region-B**

$$\frac{d^2u_{22}}{dy^2} + m\frac{dN_o}{dy} - R_2\left(\frac{du_{22}}{dy} + i\omega u_{22}\right) - \left((M_2\cos\theta)^2 + \sigma_2^2\right)u_{22} - Z_{\rho_1}R_2P_o = 0. \quad (40)$$

$$\frac{d^2N_o}{dy^2} - n\frac{du_{22}}{dy} - R_2P_j\frac{dN_s}{dy} - (2n + i\omega R_2P_j)N_o = 0.$$

$$R_2\Pr(i\omega\theta_{22} + \frac{\partial\theta_{22}}{\partial y}) = \frac{z_{k1}}{z_{\mu1}}\frac{\partial^2\theta_{22}}{\partial y^2} + 2Br\frac{\partial u_{21}}{\partial y}\frac{\partial u_{22}}{\partial y} + mBr\left(2\frac{\partial u_{21}}{\partial y}\frac{\partial u_{22}}{\partial y} + 4\frac{\partial u_{21}}{\partial y}N_o + 4\frac{\partial u_{22}}{\partial y}N_s + 8N_sN_o\right) + 2Z_\beta Br\frac{\partial N_s}{\partial y}\frac{\partial N_o}{\partial y} + 2(1+m)Br\sigma_2^2u_{21}u_{22}. \quad (41)$$

$$\frac{1}{Sc}\frac{\partial^2\Phi_{22}}{\partial y^2} + Sr\frac{\partial^2\theta_{22}}{\partial y^2} - R_2\frac{\partial\Phi_{22}}{\partial y} - R_2i\omega\Phi_{22} = 0. \quad (42)$$

- **Region-C**

$$\frac{d^4u_{32}}{dy^4} - S_2\frac{d^2u_{32}}{dy^2} + R_3S_2\frac{du_{32}}{dy} + R_3S_2i\omega u_{32} + S_2(M_3\cos\theta)^2u_{32} + S_2\sigma_3^2u_{32} - Z_{\rho_2}S_2R_3P_o = 0. \quad (43)$$

$$R_3\Pr(\frac{\partial\theta_{32}}{\partial y} + i\omega\theta_{32}) = \frac{z_{k2}}{z_{\mu2}}\frac{\partial^2\theta_{32}}{\partial y^2} + \frac{Br}{S_2}\left(\frac{\partial^2u_{32}}{\partial y^2}\right)^2 + Br\left(\frac{\partial u_{32}}{\partial y}\right)^2 + Br\sigma_3^2u_{32}^2. \quad (44)$$

$$\frac{1}{Sc}\frac{\partial^2\Phi_{32}}{\partial y^2} + Sr\frac{\partial^2\theta_{32}}{\partial y^2} - R_3\frac{\partial\Phi_{32}}{\partial y} - R_3i\omega\Phi_{32} = 0. \quad (45)$$

Oscillatory flow boundary conditions:

$$\left.\begin{aligned}
&\frac{\partial u_{12}}{\partial y} = \alpha\sigma_4\left(u_{12}' - \frac{R_1}{\sigma_4^2}P_s\right), u_{12}' = u_{12},\\
&\frac{\partial^2u_{12}}{\partial y^2} = 0, \quad \text{at} \quad y = -1.\\
&z_{\mu1}\frac{\partial u_{12}}{\partial y} - (1/S_1)z_{\mu1}\frac{\partial^3u_{12}}{\partial y^3} = (1+m)\frac{\partial u_{22}}{\partial y} + mN_o,\\
&N_o = 0, u_{12} = u_{22}, \frac{\partial u_{12}}{\partial y} = \frac{\partial u_{22}}{\partial y}, \quad \text{at} \quad y = 0.\\
&z_{\mu2}\frac{\partial u_{32}}{\partial y} - (1/S_2)z_{\mu2}\frac{\partial^3u_{32}}{\partial y^3} = (1+m)\frac{\partial u_{22}}{\partial y} + mN_o,\\
&N_o = 0, u_{22} = u_{32}, \frac{\partial u_{22}}{\partial y} = \frac{\partial u_{32}}{\partial y}, \quad \text{at} \quad y = \delta_1.\\
&\frac{\partial u_{32}}{\partial y} = -\alpha\sigma_5\left(u_{32}' - Z_{\rho1}\frac{R_3}{\sigma_5^2}P_s\right), u_{32}' = u_{32},\\
&\frac{\partial^2u_{32}}{\partial y^2} = 0, \quad \text{at} \quad y = 2.
\end{aligned}\right\} \quad (46)$$

Temperature unsteady flow boundary conditions

$$\left.\begin{aligned}
&\theta_{12} = 0, \quad \text{at} \quad y = -1.\\
&\theta_{12} = \theta_{22}, \frac{\partial\theta_{12}}{\partial y} = Z_{k1}\frac{\partial\theta_{22}}{\partial y}, \quad \text{at} \quad y = 0.\\
&\theta_{22} = \theta_{32}, \frac{\partial\theta_{22}}{\partial y} = Z_{k2}\frac{\partial\theta_{32}}{\partial y}, \quad \text{at} \quad y = 1.\\
&\theta_{32} = 0, \quad \text{at} \quad y = 2.
\end{aligned}\right\} \quad (47)$$

Unsteady flow concentration boundary conditions

$$\left.\begin{aligned}
&\Phi_{12} = 0, \quad \text{at} \quad y = -1. \\
&\Phi_{12} = \Phi_{22}, \frac{\partial \Phi_{12}}{\partial y} = Z_{D1} \frac{\partial \Phi_{22}}{\partial y}, \quad \text{at} \quad y = 0. \\
&\Phi_{22} = \Phi_{32}, \frac{\partial \Phi_{22}}{\partial y} = Z_{D2} \frac{\partial \Phi_{32}}{\partial y}, \quad \text{at} \quad y = \delta_1. \\
&\Phi_{32} = 0, \quad \text{at} \quad y = 2.
\end{aligned}\right\} \tag{48}$$

3. The problem's Solution

The pulsatile flow solution is provided for velocity, temperature, and concentration (49 - 58).

$$\left.\begin{aligned}
u_1 &= u_{11} + u_{12} e^{i\omega t}. \\
u_2 &= u_{21} + u_{22} e^{i\omega t}. \\
N &= N_s + N_o e^{i\omega t}. \\
u_3 &= u_{31} + u_{32} e^{i\omega t}.
\end{aligned}\right\} \tag{49-52}$$

$$\left.\begin{aligned}
\theta_1 &= \theta_{11} + \theta_{12} e^{i\omega t}. \\
\theta_2 &= \theta_{21} + \theta_{22} e^{i\omega t}. \\
\theta_3 &= \theta_{31} + \theta_{32} e^{i\omega t}.
\end{aligned}\right\} \tag{53-55}$$

$$\left.\begin{aligned}
\Phi_1 &= \Phi_{11} + \Phi_{12} e^{i\omega t}. \\
\Phi_2 &= \Phi_{21} + \Phi_{22} e^{i\omega t}. \\
\Phi_3 &= \Phi_{31} + \Phi_{32} e^{i\omega t}.
\end{aligned}\right\} \tag{56-58}$$

To address steady**,** oscillatory flow equations and boundary conditions (25–58), we employed the shooting technique integrated with the fourth-order Runge-Kutta (RK4) scheme (Fig. 11). This approach involved transforming all higher-order differential equations into an equivalent system of first-order equations. The shooting method was then utilised to solve the resulting system, enabling the generation of numerical results.

Key components of this methodology included the RK-4 scheme for numerical integration and Newton's method for handling nonlinear differential equations. The boundary value problem (BVP) was reformulated as an initial value problem (IVP), with missing slopes estimated iteratively (see Ref. [42]). For this study, we utilised Mathematica's built-in NDSolve function to directly compute solutions, ensuring both computational efficiency and accuracy. To enhance precision, a step size of h=0.01 and an error tolerance of 10^{-6} were employed throughout the computations.

4. Entropy Generation

Entropy generation in immiscible flows quantifies irreversible losses due to heat transfer, fluid friction, and interfacial mixing, helping optimize energy efficiency and analyze flow stability.

$$\begin{aligned}
Eg_1 &= \left(\frac{d\theta_1}{dy}\right)^2 + \frac{S_1 Br}{\Omega}\left(\frac{d^2 u_1}{dy^2}\right)^2 + \frac{Br}{\Omega}\left(\frac{du_1}{dy}\right) \\
&+ \frac{Br}{\Omega}\sigma_1^2 u_1^2 + \Lambda\frac{\pi^2}{\Omega^2}\left(\frac{d\Phi_1}{dy}\right)^2 + \Lambda\frac{\pi}{\Omega}\frac{d\Phi_1}{dy}\frac{d\theta_1}{dy}
\end{aligned} \tag{59}$$

$$\begin{aligned}
Eg_2 &= \left(\frac{d\theta_2}{dy}\right)^2 + \frac{Z_\mu}{Z_k}\frac{Br}{\Omega}\left(\frac{du_2}{dy}\right)^2 \\
&+ \frac{m}{Z_k}\frac{Br}{\Omega}\left(\frac{du_2}{dy} + 2N\right) + Z_\beta Z_\mu \frac{Br}{\Omega}\left(\frac{dN}{dy}\right)^2 \\
&+ \frac{Z_\mu}{Z_k}\frac{Br}{\Omega}\sigma_2^2 u_2^2 + \Lambda\frac{\pi^2}{\Omega^2}\left(\frac{d\Phi_2}{dy}\right)^2 \\
&+ \Lambda\frac{\pi}{\Omega}\frac{d\Phi_2}{dy}\frac{d\theta_2}{dy}
\end{aligned} \tag{60}$$

$$\begin{aligned}
Eg_3 &= \left(\frac{d\theta_3}{dy}\right)^2 + \frac{S_2 Br}{\Omega Z_{k1}}\left(\frac{d^2 u_3}{dy^2}\right)^2 \\
&+ \frac{Z_{\mu 1} Br}{\Omega}\left(\frac{du_3}{dy}\right) + \frac{Br}{\Omega}\sigma_3^2 u_3^2 \\
&+ \Lambda\frac{\pi^2}{\Omega^2}\left(\frac{d\Phi_3}{dy}\right)^2 + \Lambda\frac{\pi}{\Omega}\frac{d\Phi_3}{dy}\frac{d\theta_3}{dy}
\end{aligned} \tag{61}$$

5. Bejan Number

The Bejan number (Be) is a dimensionless parameter that represents the ratio of entropy generation due to heat transfer to the total entropy generation, helping analyze irreversibility in thermodynamic systems.

$$Be = \sum_{i=1}^{3} \frac{\left(\frac{d\theta_i}{dy}\right)^2}{Eg_i} \tag{62}$$

6. Nusselt Number

The Nusselt number measures heat transfer efficiency influenced by fluid interactions and permeability and is given by:

$$\left.\begin{aligned}
Nu_1 &= \frac{\partial \theta_1}{\partial y}, \quad \text{at} \quad y = -1. \\
Nu_2 &= \frac{\partial \theta_3}{\partial y}, \quad \text{at} \quad y = 2.
\end{aligned}\right\} \tag{63}$$

7. Shear Stress

Shear stress at both beds is given by:

$$\tau = \frac{\partial \tilde{u}}{\partial y} - \frac{\partial^3 \tilde{u}}{\partial y^3} \quad \text{at} \quad y = -1, 2 \tag{64}$$

8. Results and Discussion

This section presents the key characteristics of the heat and mass transfer process, with findings presented through graphical illustrations (figures 2-8) and a bar chart for

$(Z_{\mu 1} = 1, Z_{\mu 2} = 1.3,\ Z_{\rho 1} = 1.1, Z_{\rho 2} = 1,$

$Z_{k1} = 1,\ Z_{k1} = 0.8,\ Z_{D1} = 0.9,\ Z_{D2} = 0.8,$

$M_1 = 1, Z_\sigma = 1, \sigma = 1, \omega t = \frac{\pi}{4}, \theta = \frac{\pi}{6},$

$P_s = P_0 = 1, R_1 = 0.5, n = 4, m = 0.5,\ Z_s = 1,$

$Pr = 0.75, Br = 1, Z_\beta = 0.5, \mathrm{Sc} = 0.5,\ \ \mathrm{Sr} = 1)$

except where they are variables.

From Figure 2 (a), one can notice that an increase in the slip parameter leads to a reduction in velocity. This occurs because a slip at the boundary reduces the shear stress exerted by the surface on the fluid, weakening the momentum transfer and slowing down the flow.

Similarly, Figure 2 (b) indicates that a stronger magnetic field results in a decreased velocity. This is due to the application of the magnetic field, which induces retarding forces, commonly referred to as Lorentz forces, that oppose the flow by acting as resistive drag forces in the reverse direction.

Figure 2 (c) demonstrates that velocity rises with an increase in the Reynolds number. A higher Reynolds number implies a dominance of inertial forces over viscous forces, promoting higher fluid acceleration and greater momentum transport, thereby enhancing velocity, and Figure 2 (d) shows that the velocity falls with an increasing frequency parameter, even as permeability approaches infinity. Physically, a higher frequency parameter causes rapid oscillations in unsteady flow, resisting large velocity amplitudes and increasing inertia, which reduces overall velocity.

Furthermore, Figures 2 (e) and 2 (f) reveal that higher micropolar material and couple stress parameters, whether in porous or non-porous media, contribute to an increase in velocity. This is because the micro-rotational effects and additional stresses of micropolar and couple stress fluids enhance momentum transport, enabling higher flow velocities.

In Figure 2 (g), a greater inclination angle corresponds to an enhancement in velocity, and a greater inclination angle of the magnetic field reduces the opposing Lorentz force, allowing the fluid to flow more freely. This reduction in resistive drag leads to an increase in velocity, whereas Figure 2 (h) highlights that a higher permeability parameter causes a decline in velocity.

Lastly, unsteady velocity fluctuates over time in both slip and no-slip scenarios, as shown in Fig. 2 (i).

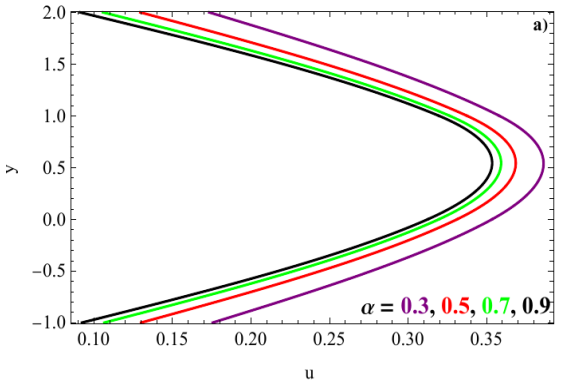

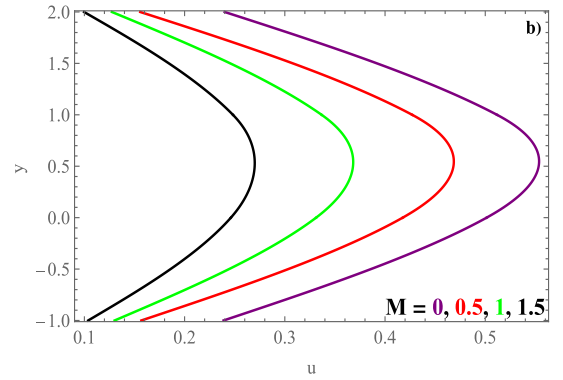

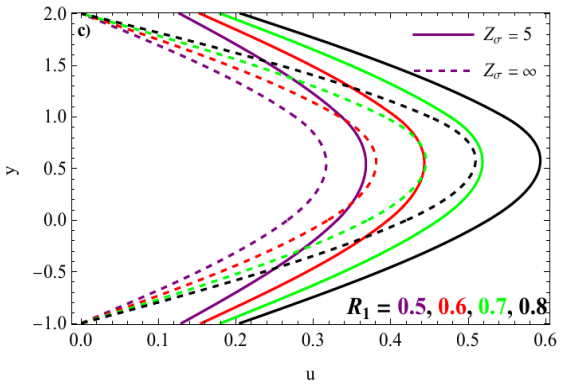

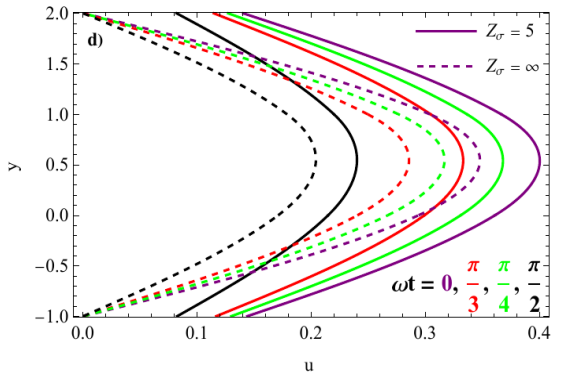

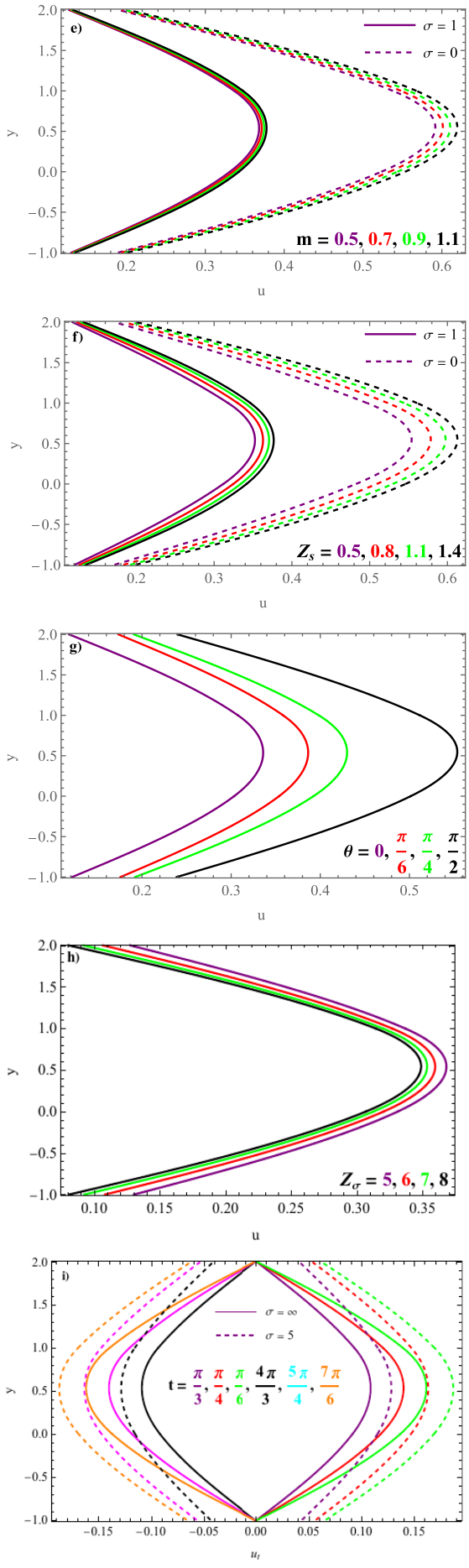

Fig. 2. Velocity variation with different parameters

Figure 3 outlines the microrotation velocity (N) variations within the core region as influenced by different parameters.

From Figure 3 (a), one can observe that N falls with the rise of the micropolar material parameter.

Figure 3 (b) indicates that a higher Hartmann number raises N near (y = 0) due to suppressed velocity gradients enhancing rotational effects, but lowers it near ($y = \delta_1$) as the magnetic field dampens both translational and rotational motions.

In Figure 3 (c), an increase in the slip parameter leads to a rise in N at the upper interface ($y = \delta_1$) and a fall at the lower interface (y = 0).

Figure 3 (d) reveals that increasing the frequency parameter causes N to rise when it reaches (y = 0) and to drop near ($y = \delta_1$).

Figure 3 (e) shows a decline in N with an increase in the microrotation parameter.

Figure 3 (f) highlights that higher gyration parameters enhance N near ($y = \delta_1$) and reduce it at (y = 0).

Similarly, in Figure 3 (g), a rise in permeability decreases N near (y = 0) while it enhances it near ($y = \delta_1$).

Figure 3 (h) shows that as the inclination angle grows, N rises near ($y = \delta_1$) and falls near (y = 0).

Lastly, Figure 3 (i) captures the unsteady microrotation velocity, demonstrating its oscillatory nature over time.

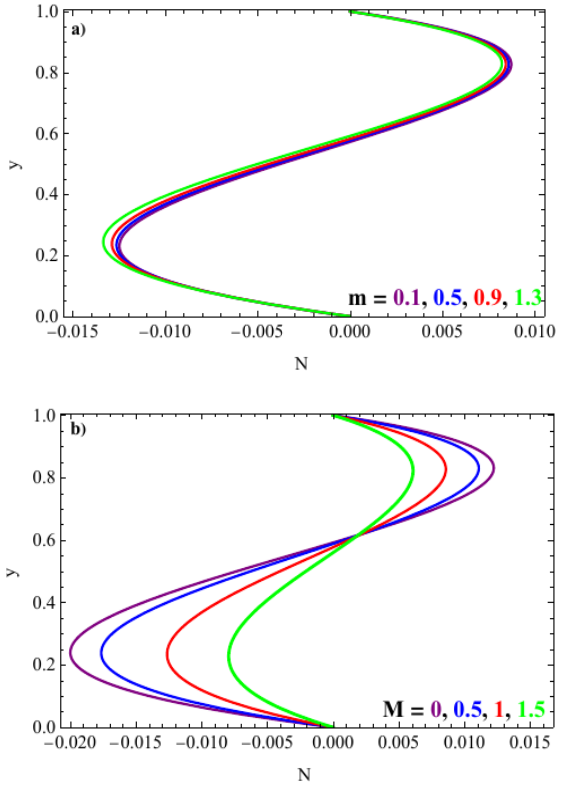

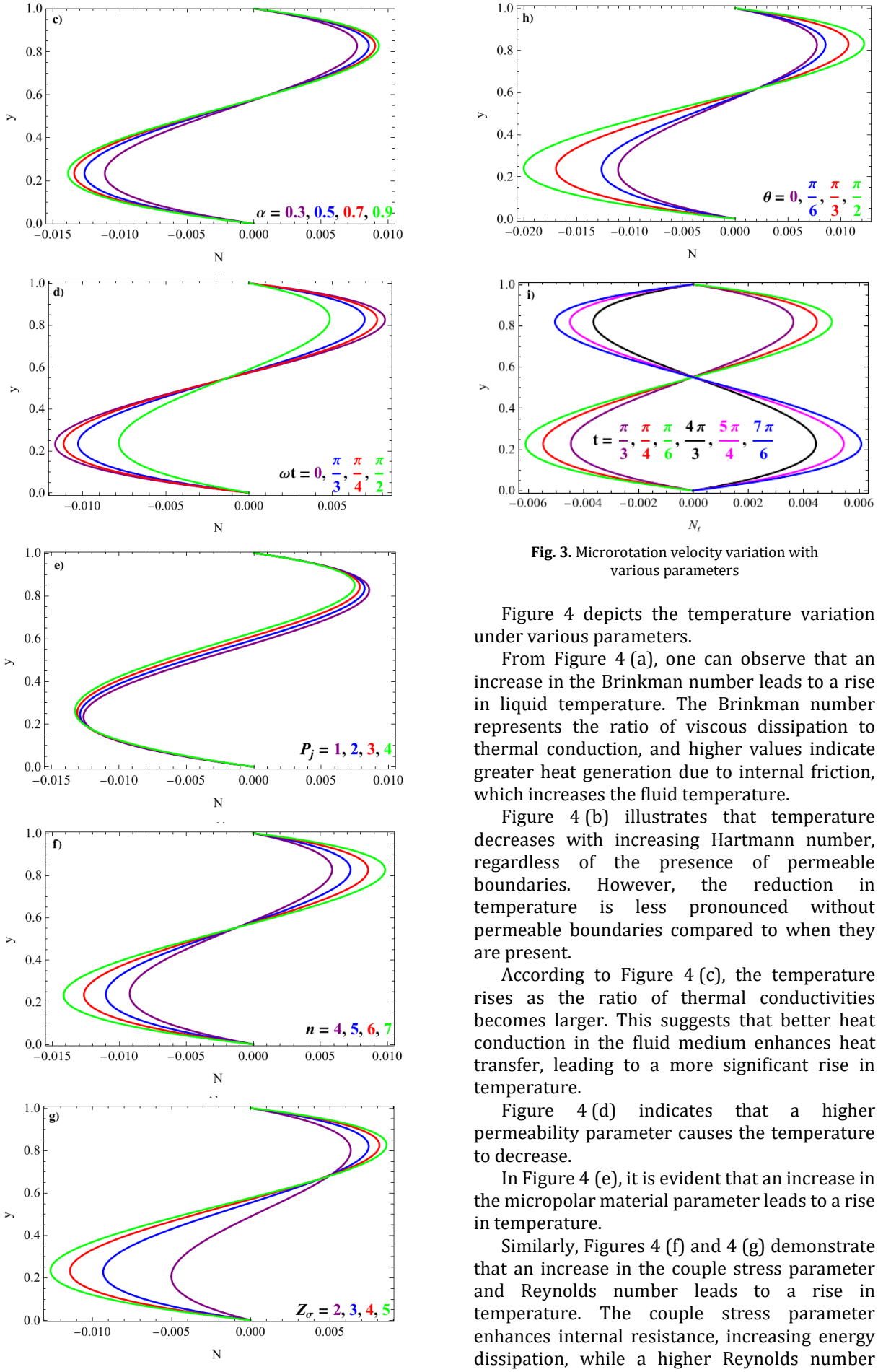

Fig. 3. Microrotation velocity variation with various parameters

Figure 4 depicts the temperature variation under various parameters.

From Figure 4 (a), one can observe that an increase in the Brinkman number leads to a rise in liquid temperature. The Brinkman number represents the ratio of viscous dissipation to thermal conduction, and higher values indicate greater heat generation due to internal friction, which increases the fluid temperature.

Figure 4 (b) illustrates that temperature decreases with increasing Hartmann number, regardless of the presence of permeable boundaries. However, the reduction in temperature is less pronounced without permeable boundaries compared to when they are present.

According to Figure 4 (c), the temperature rises as the ratio of thermal conductivities becomes larger. This suggests that better heat conduction in the fluid medium enhances heat transfer, leading to a more significant rise in temperature.

Figure 4 (d) indicates that a higher permeability parameter causes the temperature to decrease.

In Figure 4 (e), it is evident that an increase in the micropolar material parameter leads to a rise in temperature.

Similarly, Figures 4 (f) and 4 (g) demonstrate that an increase in the couple stress parameter and Reynolds number leads to a rise in temperature. The couple stress parameter enhances internal resistance, increasing energy dissipation, while a higher Reynolds number

amplifies shear stress, leading to greater viscous heating.

Figure 4 (h) illustrates that an increase in the inclination angle leads to a temperature rise.

Finally, Figure 4 (i) highlights that the unsteady temperature fluctuates over time.

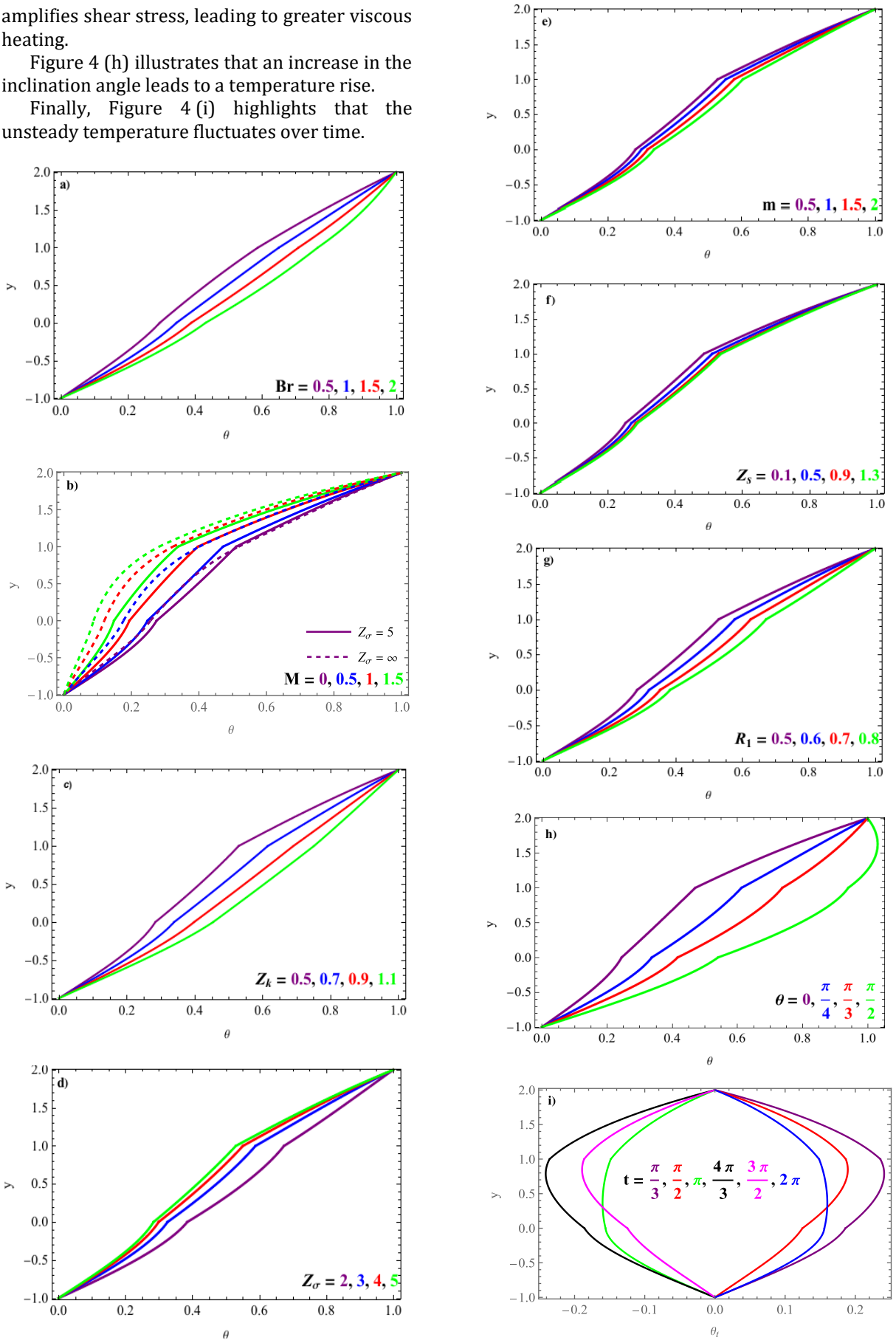

Fig. 4. Temperature distribution with various parameters

Figure 5 depicts the concentration variation under different parameters.

From Figure 5 (a), one can notice that a higher Schmidt number limits mass diffusion, lowering the concentration.

Figure 5 (b) shows that a higher Soret number also leads to a reduction in concentration as thermal diffusion drives lighter species away.

According to Figure 5 (c), the concentration increases as the ratio of diffusion coefficients becomes larger.

Finally, Figure 5 (d) highlights the unsteady concentration, which exhibits fluctuations over time due to transient mass transport effects.

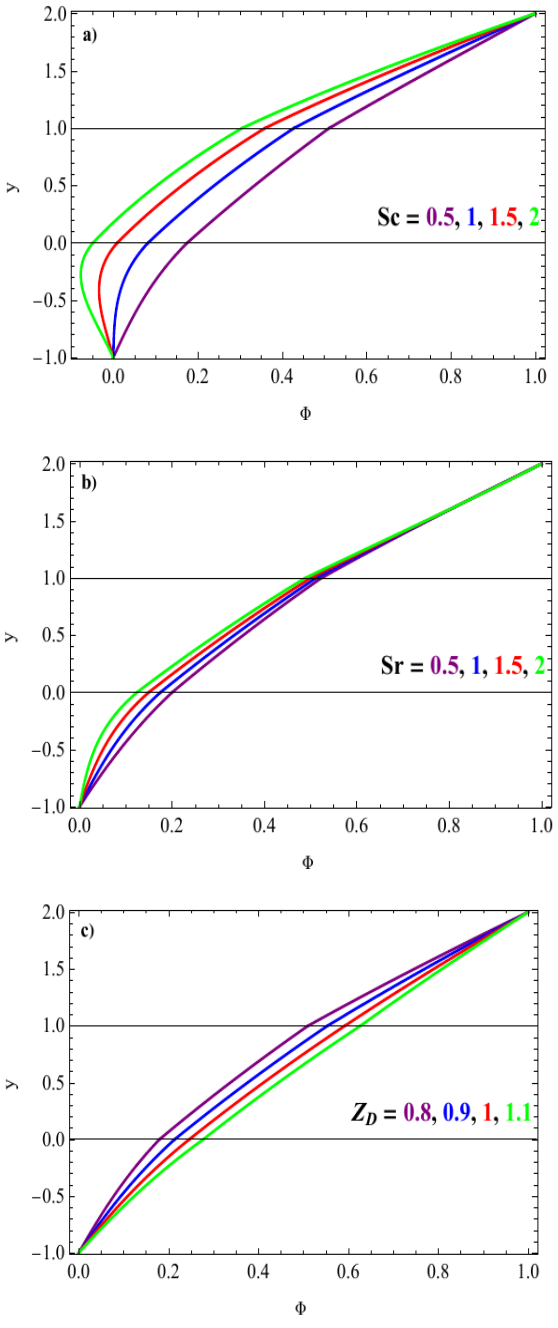

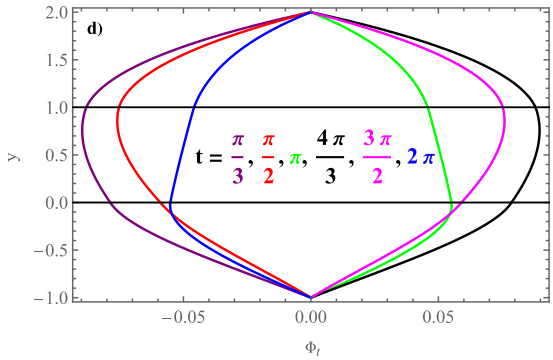

Fig. 5. Concentration variation with several parameters

Figure 6 shows the changes in the Nusselt number under varying parameters.

As seen in Figures 6 (a) and 6 (b), increasing permeability decreases the Nusselt number at the LPB due to reduced temperature gradients but enhances heat transport at the UPB via convection.

Figures 6 (c) and 6 (d) indicate that a higher Hartmann number suppresses convective heat transfer at the LPB due to magnetic damping but stabilises the flow and improves heat transfer at the UPB.

Figures 6 (e) and 6 (f) illustrate that higher Reynolds numbers enhance convective mixing and heat transfer at the LPB but destabilise the thermal boundary layer at the UPB, reducing the Nusselt number.

Similarly, Figures 6 (g) and 6 (h) demonstrate that higher Brinkman numbers increase viscous dissipation at the LPB, boosting heat transfer, but reduce the thermal gradient at the UPB, lowering heat transfer rates.

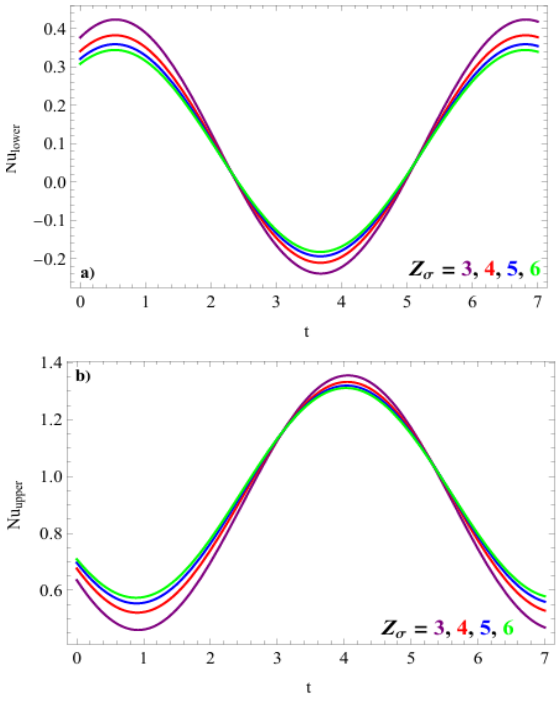

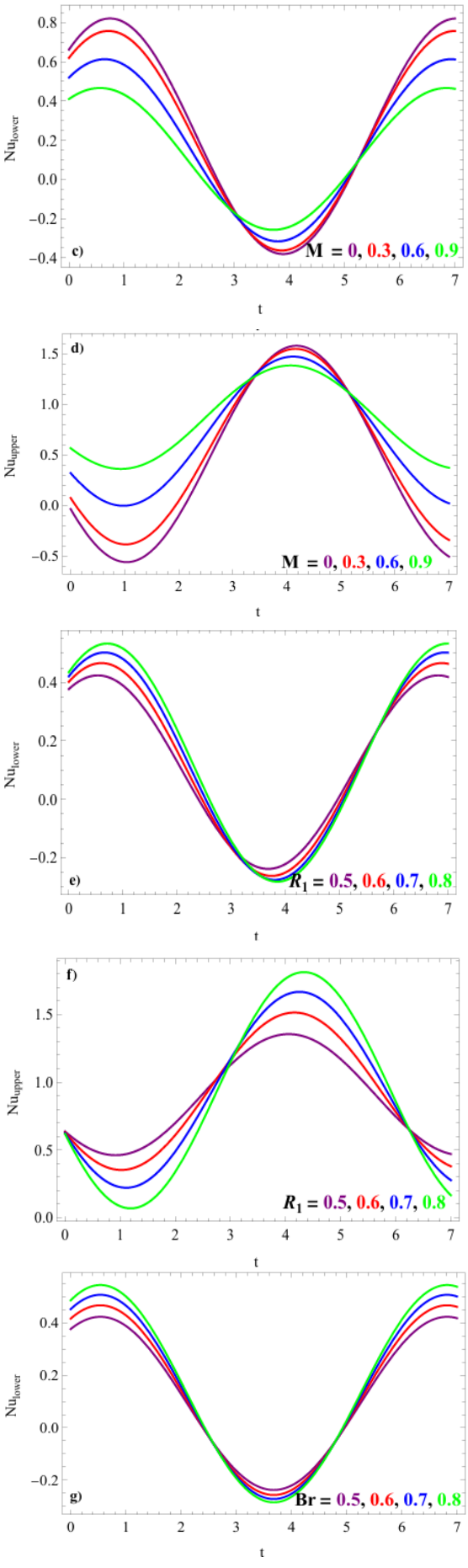

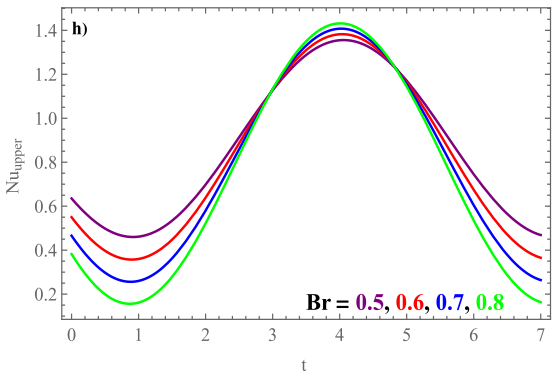

Fig. 6. Nusselt number variation with pertinent parameters for ($Z_{\mu 2} = 1.1,\ Z_{k2} = 0.8, M_1 = 0.5, Z_\sigma = 5,$ $\sigma = 0.5, n = 0.5, m = 0.5,$)

Figure 7 shows entropy generation influenced by various parameters using 2D and 3D plots.

Figures 7 (a) and 7 (e) demonstrate that entropy generation exhibits an increasing trend with a rise in the Brinkman number, as higher viscous dissipation leads to greater heat production and irreversibilities within the system.

Figures 7 (b) and 7 (f) illustrate that a higher dimensionless temperature difference parameter enhances the heat transfer driving force, reducing irreversible losses and lowering entropy generation. This reflects improved thermal efficiency in the system.

Figures 7 (c) and 7 (g) demonstrate that an increase in the Hartmann number reduces entropy generation. This implies that the Lorentz force generated by the magnetic field suppresses velocity gradients, leading to a reduction in entropy generation due to fluid friction.

Figures 7 (d) and 7 (h) illustrate that an increase in the slip parameter reduces entropy generation by weakening the no-slip condition at the boundary, thereby diminishing frictional effects and viscous dissipation near the walls, leading to lower irreversibilities in the system.

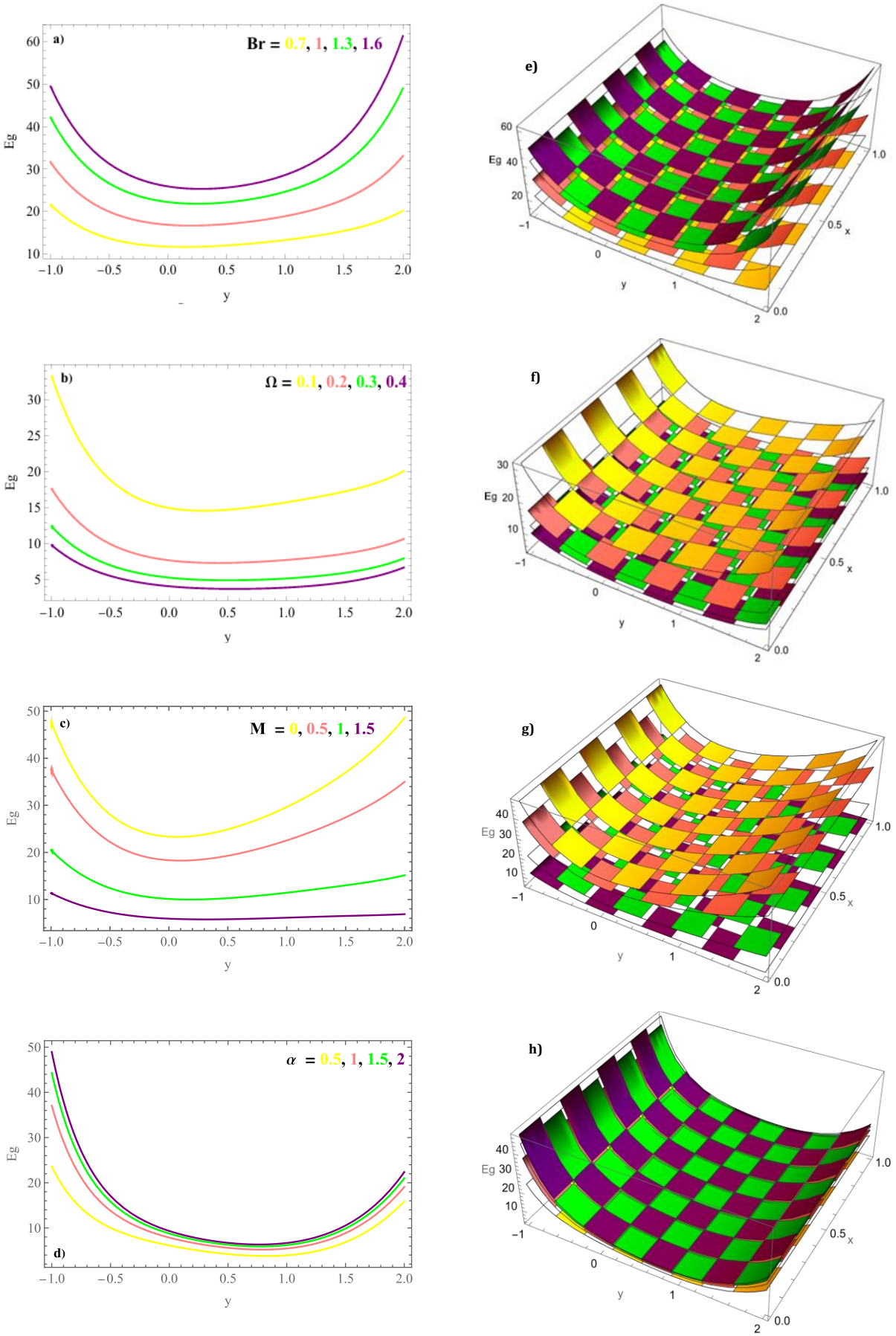

Fig. 7. Variation of entropy generation with different parameters using 2D and 3D plots for ($Z_{\mu 2} = 0.9,\ Z_{\rho 1} = 1.2, Z_{\rho 2} = 0.7,\ Z_{k1} = Z_{k2} = 1.5,\ Z_{D1} = 1.4,\ Z_{D2} = 1, M_1 = 0.5,\ Z_\sigma = 5, \sigma = 1.7, \omega t = \frac{\pi}{6},\ P_s = P_0 = 0.7,\ \theta = \frac{\pi}{6}, R_1 = 0.5, n = 0.5, \Lambda = 1, \Omega = 0.1, \Pi = 0.5$).

Figure 8 shows parameter effects on the Bejan number through 2D and 3D plots.

In Figures 8 (a) and 8 (e), which depict the variation of the Bejan number with Brinkman number (Br), one can observe that with the rise of the Brinkman number, the Bejan number approaches 1, suggesting that heat transfer becomes the dominant source of irreversibility.

Figures 8 (b) and 8 (f) show that increasing the dimensionless temperature difference parameter raises the Bejan number, indicating dominant heat transfer irreversibility. This highlights the significant role of temperature gradients in entropy generation.

Figures 8 (c) and 8 (g) show that increasing the Hartmann number enhances the Lorentz force, suppressing velocity gradients and reducing friction-induced entropy, thereby increasing the Bejan number due to heat transfer dominance.

Finally, Figures 8 (d) and 8 (h) show that with an increase in the slip parameter, the Bejan number decreases near the walls due to reduced frictional irreversibilities, while it increases in the middle zone as thermal irreversibilities gain dominance over viscous effects. This highlights the contrasting influence of slip conditions across different regions of the flow.

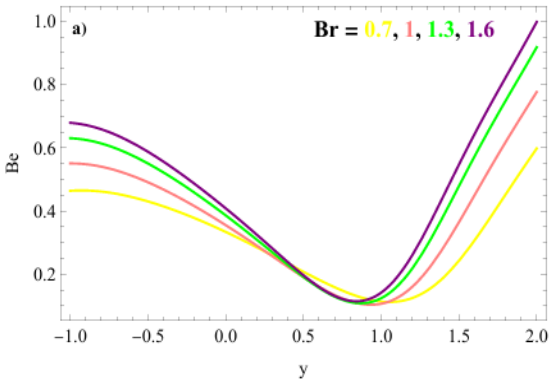

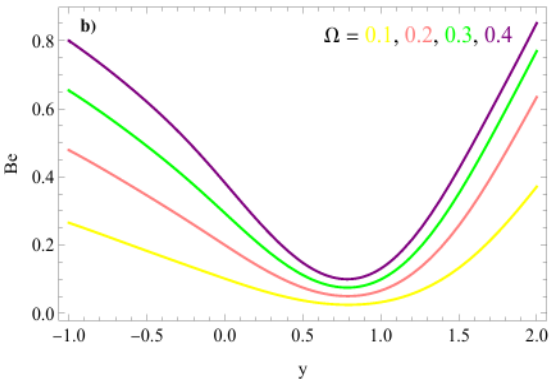

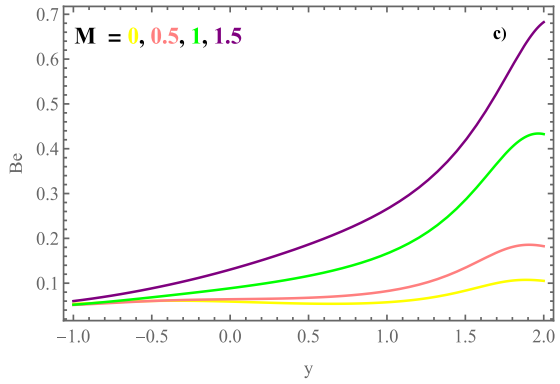

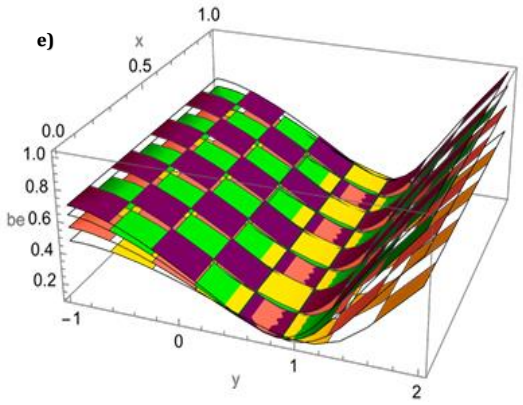

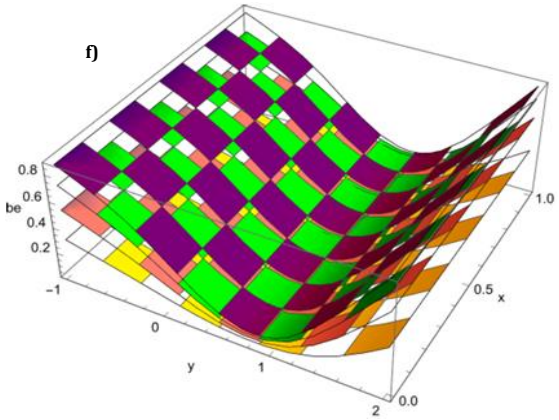

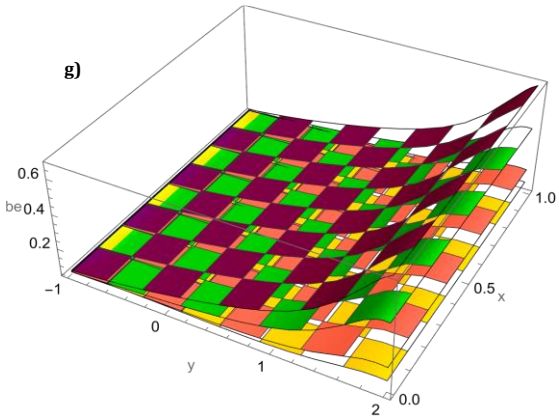

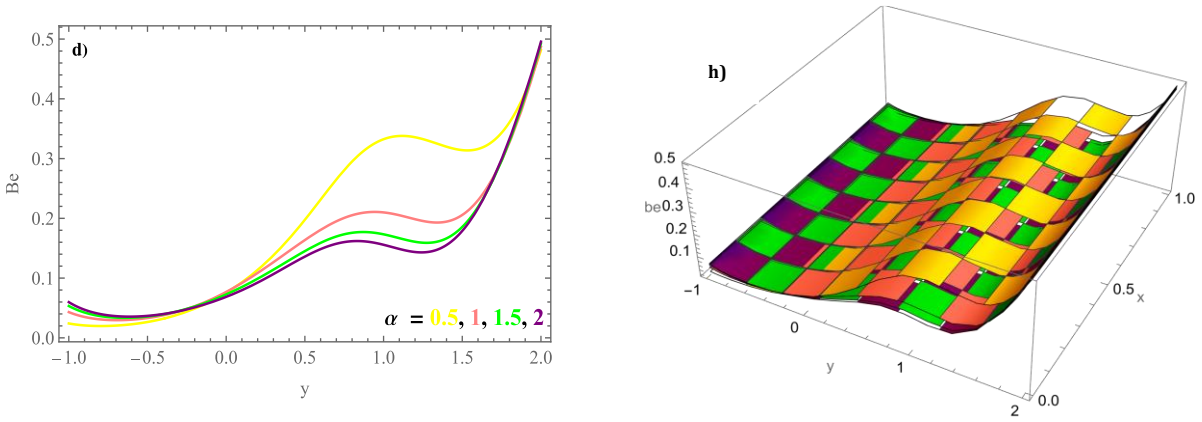

Fig. 8. Bejan number variation with various parameters using 2D and 3D plots. ($Z_{\mu 2} = 0.9,\ Z_{\rho 1} = 1.2, Z_{\rho 2} = 0.7, Z_{k1} = Z_{k2} = 1.5,\ Z_{D1} = 1.4,\ Z_{D2} = 1, M_1 = 0.5,\ Z_\sigma = 5, \sigma = 1.7, \omega t = \frac{\pi}{6},\ P_s = P_0 = 0.7,\ \theta = \frac{\pi}{6}, R_1 = 0.5, n = 0.5, \Lambda = 1, \Omega = 0.1, \Pi = 0.5$).

Figure 9 illustrates the variation in shear stress under different parameters at both permeable beds.

In Figure 9 (a), the shear stress rises with an increase in the slip parameter.

Conversely, Figure 9 (b) shows that increasing the Hartmann number reduces shear stress at both beds due to the damping effect of the magnetic field. The Lorentz force suppresses velocity gradients, leading to lower wall friction.

Figure 9 (c) highlights that a rise in the permeability parameter leads to an increase in shear stress at both permeable beds.

Similarly, Figures 9 (d) illustrate that as the Reynolds number increases, the shear stress at both permeable beds rises, attributed to enhanced inertial forces overcoming viscous resistance.

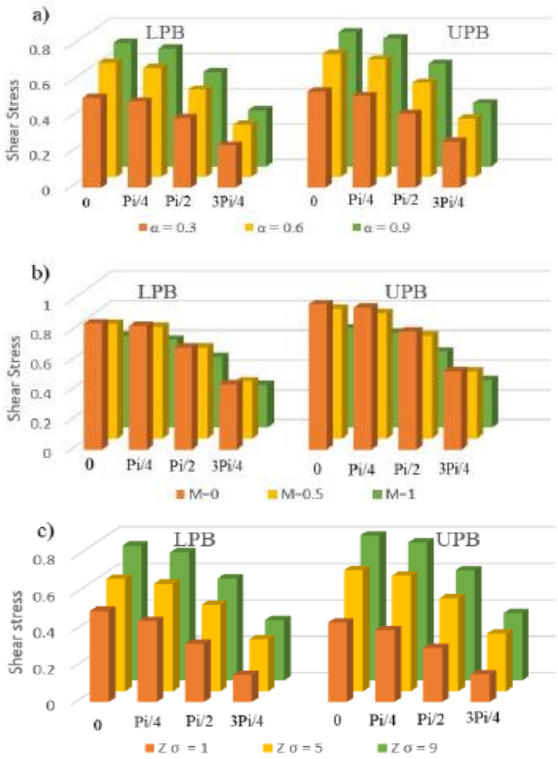

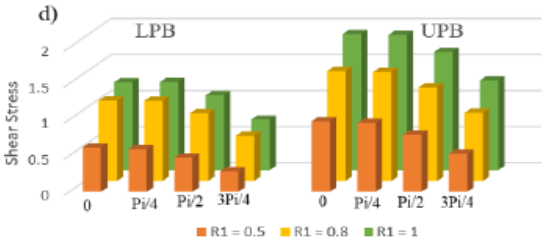

Fig. 9. Shear Stress distribution with different parameters

Figure 10 presents a comparative analysis of velocity, temperature, and shear stress.

Figure 10 (a) illustrates that when the permeability and couple-stress fluid parameters approach infinity with the absence of porosity, and inclination angle ($Z_s = Z_\sigma = \infty,\ \sigma = \theta = 0$). The results of the present study align with those reported by [2], while the findings of [1] are recovered in the absence of the micropolar, gyration, and microrotation parameters, demonstrating excellent agreement in the velocity profile.

Figure 10 (b) demonstrates that the temperature profile aligns with Reference [1] by exhibiting suppressed values ($Z_s = Z_\sigma = \infty,\ \sigma = \theta = m = n = P_j = Ec = 0$).

The variation of shear stress with respect to the Hartmann number and micropolar material parameter demonstrates good agreement with the results provided in reference [2], as illustrated in Table 1.

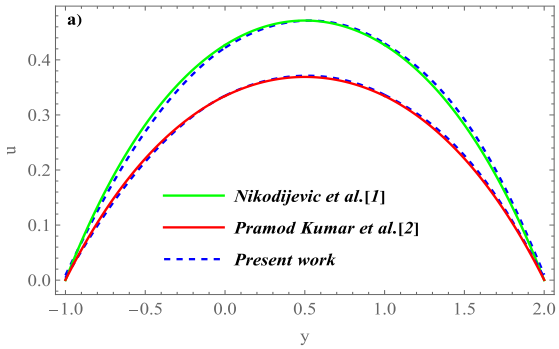

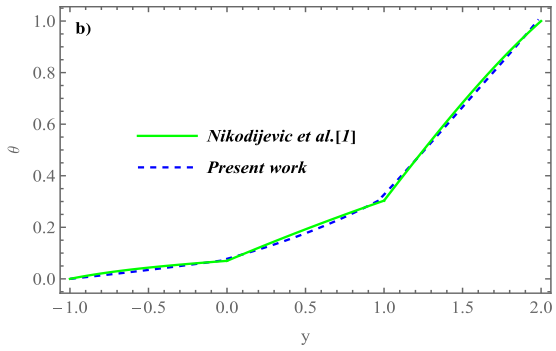

Fig. 10. Comparative study

Table 1. Shear stress

Present work		Pramod Kumar et al.[2]
M	τ(upper)	τ(upper)
1	0.4828	0.4828
3	0.2214	0.2214
5	0.1373	0.1373
$m = 0.08$	0.4812	0.4812
1	0.4828	0.4828
2	0.4835	0.4835

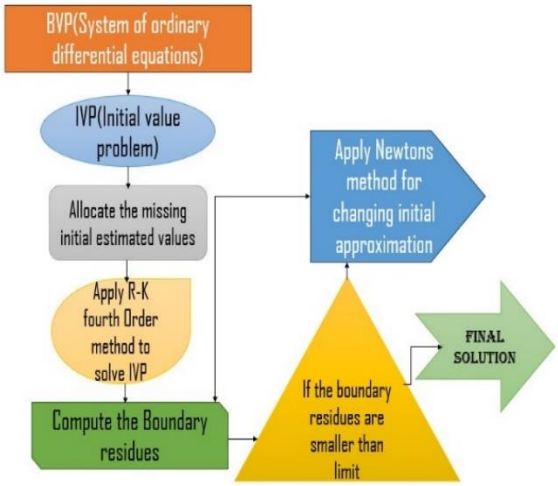

Fig. 11. Flow Chart for Shooting technique

9. Conclusions

This study explores the flow of micropolar and couple stress immiscible liquids between permeable beds, focusing on entropy generation. In this model, the flow is divided into three Regions: Region A and C are occupied by couple stress liquids, while Region-B contains a micropolar liquid. The Darcy law and the B-J slip conditions are implemented at the liquid-permeable bed interfaces. Assuming that the flow is subjected to a periodic pressure gradient and is fully developed, the velocity, microrotation velocity, temperature, and concentration are separated into steady and oscillatory components. The equations that govern the flow have been solved numerically by using the RK-4th order method with the shooting technique in Mathematica software. The resulting graphs reveal the influence of various parameters on velocity, microrotation-velocity, temperature, concentration distributions, Nusselt number, entropy generation, Bejan number, and shear stress have been presented and analysed. The results of this investigation are summarised as follows:

- Flow suppression is influenced by the Hartmann number, slip, permeability, and frequency parameters, while the Reynolds number, couple stress parameter, inclination angle, and micropolar fluid material parameter promote flow intensification.
- The microrotation velocity increases near the $(y = \delta_1)$ and decreases near the $(y = 0)$ of the central region, influenced by parameters such as porosity, slip, and inclination angle.
- Within the core region of the channel, the microrotation velocity decreases near the upper interface of Region-B, where the couple stress fluid flows, but increases near the lower interface with higher Hartmann and frequency parameter values.
- An increase in micropolar, couple stress and microrotation parameters decreases microrotation velocity within the core region.
- When the Brinkman number, Reynolds number, inclination angle, thermal conductivity ratio, and micropolar material parameter rise, the temperature distribution increases. In contrast, raising the Hartmann number and permeability results in a decline in temperature distribution.
- A rise in the Schmidt and Soret numbers, results in a reduction of concentration, whereas a higher diffusivity ratio leads to a fall in liquid concentration.
- Entropy generation increases with the Brinkman number, while a higher temperature difference parameter reduces it.
- The Bejan number rises with the Brinkman number and the dimensionless temperature difference parameter.
- As the permeability parameter and Hartmann number increase, the rate of heat transfer falls at the LPB and enhances at the UPB. On the other hand, with higher Brinkman and Reynolds numbers, the rate of heat transfer rises at the LPB and diminishes at the UPB.
- Shear stress rises with increasing slip, permeability, and Reynolds number. In contrast, it diminishes as the Hartmann number increases.

- In the absence of the inclination angle, porosity, and when taking the permeability and couple-stress parameters to infinity, our results show strong agreement with the findings of [2]. Furthermore, when the micropolar material, gyration, and microrotation parameters are also neglected, the results align with those of Ref. [1].

Nomenclature

D_j	Diffusion coefficient
ρ_j	Density
μ_j	Viscosity
$B_0 Cos\theta$	Inclined magnetic field
k_j	Thermal conductivity
R_j	Reynolds number
Λ	Diffusion parameter
σ_{*j}	Electrical conductivity
P_j	Micropolar parameter
α	Slip parameter
M_j	Hartmann number
η_j, Sj	Couple stress parameters
$Br = Ec * Pr$	Brinkman number
N	Microrotation velocity
u_j	Velocity
C_{pj}	Specific heat
m, n, Z_β	Micropolar parameters
V	Suction and injection parameter
C_j	Concentration
Sr	Soret number
Sc	Schmidt number
u_1', u_3'	Slip velocities
x, y	Coordinates of the channel
T_{w1}, T_{w2}	Temperature at both beds
C_{w1}, C_{w2}	Fluid Concentration
Z_{D1}, Z_{D2}	Ratio of diffusion
Z_{k1}, Z_{k2}	Ratio of thermal conductivity
$Z_{\mu 1}, Z_{\mu 2}$	Ratio of viscosity
$Z_{\rho 1}, Z_{\rho 2}$	Ratio of density
Z_σ-	Permeability within beds
σ, σ_i	Porosity parameters
Ω	Dimensionless temperature diff.
Π	Dimensionless concentration diff.
LPB	Lower Permeable Bed
UPB	Lower Permeable Bed
S_1, S_2	Couple stress parameter

Funding Statement

The author acknowledges the financial support received through research scholarship from VIT-AP University, Amaravathi-522237, INDIA..

Conflicts of Interest

The author declares that there is no conflict of interest regarding the publication of this article.

Authors Contribution Statement

Madhurya Vangalapudi: Conceptualization; Methodology; Investigation; Validation; Visualization; Writing – Original Draft.

Suripeddi Srinivas: Supervision; Writing – Review & Editing; Validation.

References

[1] Nikodijević, D. D., Stamenković, Ž. M., Jovanović, M. M., Kocić, M. M., & Nikodijević, J. D., 2014. Flow and heat transfer of three immiscible fluids in the presence of uniform magnetic field. *Thermal science*, *18*(3), pp. 1019-1028. https://doi.org/10.2298/TSCI1403019N

[2] Kumar Yadav, P., Jaiswal, S., Asim, T., & Mishra, R., 2018. Influence of a magnetic field on the flow of a micropolar fluid sandwiched between two Newtonian fluid layers through a porous medium. *The European Physical Journal Plus*, *133*(7), 247. DOI 10.1140/epjp/i2018-12071-5

[3] Wang, C. Y., 1971. Pulsatile flow in a porous channel. *Journal of Applied Mechanics,* pp. 553-555. https://doi.org/10.1115/1.3408822

[4] Radhakrishnamacharya, G., & Maiti, M. K., 1977. Heat transfer to pulsatile flow in a porous channel. *International Journal of Heat and Mass Transfer*, *20*(2), pp. 171-173. https://doi.org/10.1016/0017-9310(77)90009-6

[5] Li, B., Zheng, L., Zhang, X., & Ma, L., 2008. The multiple solutions of laminar flow in a uniformly porous channel with suction/injection. *Advanced Studies in Theoretical Physics*, *2*(10), pp. 473-478.

[6] Umavathi, J. C., Kumar, J. P., & Chamkha, A. J., 2009. Convective flow of two immiscible viscous and couple stress permeable fluids through a vertical channel. *Turkish Journal of Engineering and Environmental Sciences*, *33*(4), pp. 221-243. doi:10.3906/muh-0905-29

[7] Makinde, O. D., & Chinyoka, T., 2013. Numerical investigation of buoyancy effects on hydromagnetic unsteady flow through a porous channel with suction/injection. *Journal of Mechanical Science and Technology*, *27*(5), pp. 1557-1568. DOI 10.1007/s12206-013-0221-9

[8] Eegunjobi, A. S., & Makinde, O. D., 2012. Effects of Navier slip on entropy generation in a porous channel with suction/injection. *Journal of Thermal Science and Technology*, *7*(4), pp. 522-535. DOI: 10.1299/jtst.7.522.

[9] Srinivas, S., Malathy, T., & Reddy, A. S., 2016. A note on thermal-diffusion and chemical reaction effects on MHD pulsating flow in a porous channel with slip and convective boundary conditions. *Journal of King Saud University-Engineering Sciences*, *28*(2), pp. 213-221. https://doi.org/10.1016/j.jksues.2014.03.011

[10] Srinivas, S., Kumar, C. K. K., & Reddy, A. S. S., 2018. Pulsating flow of Casson fluid in a porous channel with thermal radiation, chemical reaction and applied magnetic field. *Nonlinear Analysis: Modelling and Control*, *23*(2), pp. 213-233. https://doi.org/10.15388/NA.2018.2.5

[11] Umavathi, J. C., & Bég, O. A., 2020. Effects of thermophysical properties on heat transfer at the interface of two immiscible fluids in a vertical duct: Numerical study. *International Journal of Heat and Mass Transfer*, *154*, 119613. https://doi.org/10.1016/j.ijheatmasstransfer.2020.119613

[12] Padma Devi, M., & Srinivas, S., 2022. Thermal characteristics on two immiscible fluid flows in a porous space with time dependent pressure gradient. *Proceedings of the Institution of Mechanical Engineers, Part E: Journal of Process Mechanical Engineering*, *236*(6), pp. 2480-2490. https://doi.org/10.1177/09544089221096569

[13] Goyal, K., & Srinivas, S., 2024. Pulsatile flow of immiscible ternary hybrid nanofluid in a corrugated curved channel. *Numerical Heat Transfer, Part A: Applications*, pp. 1-29. https://doi.org/10.1080/10407782.2024.2360090

[14] Trevisan, O. V., & Bejan, A., 1987. Combined heat and mass transfer by natural convection in a vertical enclosure. *The American Society of Mechanical Engineers*, pp. 104-112. https://doi.org/10.1115/1.3248027

[15] Al-Amiri, A. M., Khanafer, K. M., & Pop, I., 2007. Numerical simulation of combined thermal and mass transport in a square lid-driven cavity. *International journal of thermal sciences*, *46*(7), pp. 662-671. https://doi.org/10.1016/j.ijthermalsci.2006.10.003

[16] Umavathi, J. C., Kumar, J. P., & Sheremet, M. A., 2017. Heat and mass transfer in a vertical double passage channel filled with electrically conducting fluid. *Physica A: Statistical Mechanics and its Applications*, *465*, pp. 195-216. https://doi.org/10.1016/j.physa.2016.07.073

[17] Cai, L., Mi, S., Luo, C., & Liu, Z., 2022. Numerical investigation on heat and mass transfer characteristics of ice slurry in pulsating flow. *International Journal of Heat and Mass Transfer*, *189*, 122722. https://doi.org/10.1016/j.ijheatmasstransfer.2022.122722

[18] Srinivas, J., & Ramana Murthy, J. V., 2016. Second law analysis of the flow of two immiscible micropolar fluids between two porous beds. *Journal of Engineering thermophysics*, *25*(1), pp. 126-142. DOI: 10.1134/S1810232816010124

[19] Thamizharasan, T., & Reddy, A. S., 2022. Entropy Generation on Pulsatile Hydromagnetic Flow of Jeffrey Nanofluid in a Porous Channel with Brownian Motion,

Thermophoresis, and Heat Source/Sink Using Cattaneo-Christov Heat Flux. *Indian Journal of Pure & Applied Physics*, *60*(8). https://doi.org/10.56042/ijpap.v60i8.63440

[20] Yadav, P. K., & Yadav, N., 2023. Entropy generation analysis in micropolar-couple stress fluid's flow in an inclined porous channel using Homotopy Analysis Method. *Chinese Journal of Physics*, *86*, pp. 469-496. https://doi.org/10.1016/j.cjph.2023.10.024

[21] Padma Devi, M., Srinivas, S., & Vajravelu, K., 2024. Entropy generation in two-immiscible MHD flow of pulsating Casson fluid in a vertical porous space with Slip effects. *Journal of Thermal Analysis and Calorimetry*, *149*(14), pp. 7449-7468.. https://doi.org/10.1007/s10973-024-13337-8

[22] Goyal, K., & Srinivas, S., 2024. Pulsatile flow of Casson hybrid nanofluid between ternary-hybrid nanofluid and nanofluid in an inclined channel with temperature-dependent viscosity. *Numerical Heat Transfer, Part A: Applications*, pp. 1-30. https://doi.org/10.1080/10407782.2024.2314735

[23] Yadav, P. K., Jaiswal, S., Verma, A. K., & Chamkha, A. J., 2023. Magnetohydrodynamics of immiscible Newtonian fluids in porous regions of different variable permeability functions. *Journal of Petroleum Science and Engineering*, *220*, 111113. https://doi.org/10.1016/j.petrol.2022.111113

[24] Vyas, P., Kasana, R.K. and Gajanand, 2025. Entropy generation in free convective micropolar couple stress regime in vertical channel. *Numerical Heat Transfer, Part A: Applications*, 86(10), pp.3033-3064. https://doi.org/10.1080/10407782.2023.2299283

[25] Jat, K., Sharma, K., Choudhary, P., & Soni, P. (2025). Entropy generation analysis of couple stress Casson fluid flow through non-permeable stretching channel. *The European Physical Journal Special Topics*, 1-20. https://doi.org/10.1140/epjs/s11734-025-01525-y

[26] Vaishnav, B. K., Choudhary, S., Choudhary, P., Jat, K., Loganathan, K., & Eswaramoorthi, S., 2025. Computational analysis of radiative micropolar fluid flow over a curved stretching sheet with viscous dissipation. *Discover Applied Sciences*, *7*(5), 451. https://doi.org/10.1007/s42452-025-06983-6

[27] Loganathan, K., Choudhary, P., Eswaramoorthi, S., Senthilvadivu, K., & Jain, R., 2025. Irreversibility analysis of bioconvective Walters' B nanofluid flow over an electromagnetic actuator with Cattaneo-Christov model. *Discover Applied Sciences*, *7*(5), 463. https://doi.org/10.1007/s42452-025-06893-7

[28] Vajravelu, K., Sreenadh, S., & Arunachalam, P. V., 1992. Combined free and forced convection in an inclined channel with permeable boundaries. *Journal of Mathematical analysis and Applications*, *166*(2), pp. 393-403. https://doi.org/10.1016/0022-247X(92)90306-X

[29] Vajravelu, K., Arunachalam, P. V., & Sreenadh, S., 1995. Unsteady flow of two immiscible conducting fluids between two permeable beds. *Journal of mathematical analysis and applications*, *196*(3), pp. 1105-1116. https://doi.org/10.1006/jmaa.1995.1463

[30] Avinash, K., Rao, J. A., Sreenadh, S., & Kumar, Y. R., 2011. Pulsatile flow of a viscous stratified fluid of variable viscosity between permeable beds. *Journal of Porous Media*, *14*(12). DOI: 10.1615/JPorMedia.v14.i12.60

[31] Iyengar, T. K. V., & Bitla, P., 2013. Pulsating flow of an incompressible micropolar fluid between permeable beds with an imposed uniform magnetic field. *Journal of Porous Media*, *16*(4). DOI: 10.1615/JPorMedia.v16.i4.30

[32] Malathy, T., & Srinivas, S., 2008. Pulsating flow of a hydromagnetic fluid between permeable beds. *International Communications in Heat and Mass Transfer*, *35*(5), pp. 681-688. https://doi.org/10.1016/j.icheatmasstransfer.2007.12.006

[33] Bitla, P., & Iyengar, T. K. V., 2014. Pulsating flow of an incompressible micropolar fluid between permeable beds with an inclined uniform magnetic field. *European Journal of Mechanics-B/Fluids*, *48*, pp. 174-182. https://doi.org/10.1016/j.euromechflu.2014.06.002

[34] Kumar, D., & Agarwal, M., 2021. MHD pulsatile flow and heat transfer of two immiscible couple stress fluids between permeable beds. *Kyungpook Mathematical Journal*, *61*(2), pp. 323-351.

https://doi.org/10.5666/KMJ.2021.61.2.323

[35] Mukherjee, S., & Shit, G. C., 2022. Mathematical modeling of electrothermal couple stress nanofluid flow and entropy in a porous microchannel under injection process. *Applied Mathematics and Computation*, *426*, 127110. https://doi.org/10.1016/j.amc.2022.127110

[36] Beavers, G. S., & Joseph, D. D., 1967. Boundary conditions at a naturally permeable wall. *Journal of fluid mechanics*, *30*(1), pp. 197-207. https://doi.org/10.1017/S0022112067001375

[37] Stokes, V. K., 1984. Couple stresses in fluids. *In Theories of fluids with microstructure: an introduction* (pp. 34-80). Berlin, Heidelberg: Springer Berlin Heidelberg.

[38] Eringen, A. C., 1966. Theory of micropolar fluids. *Journal of mathematics and Mechanics*, pp. 1-18.

[39] Eringen, A. C., 2001. *Microcontinuum field theories: II. Fluent media* (Vol. 2). Springer Science & Business Media.

[40] Lukaszewicz, G., 2012. *Micropolar fluids: theory and applications*. Springer Science & Business Media.

[41] Stokes, V. K., 2012. *Theories of fluids with microstructure: An introduction*. Springer Science & Business Media.

[42] Goyal, K., & Srinivas, S., 2023. Entropy generation analysis for hydromagnetic two-layered pulsatile immiscible flow with Joule heating and first-order chemical reaction. *Case Studies in Thermal Engineering*, *47*, 103046. https://doi.org/10.1016/j.csite.2023.103046